Ensemble quantitation of absolute metabolite concentrations in T cells reveals conserved features of immunometabolism

Samantha O'Keeffe[1], Harin Sim[2], Elle McCue[3], Junyoung O. Park[1,2]*

[1] Department of Chemical and Biomolecular Engineering, University of California, Los Angeles, Los Angeles, CA 90095, USA.

[2] Department of Bioengineering, University of California, Los Angeles, Los Angeles, CA 90095, USA.

[3] Department of Mechanical and Aerospace Engineering, University of California, Los Angeles, Los Angeles, CA 90095, USA.

* Correspondence to J.O.P. (jop@ucla.edu)

Abstract

Cells regulate metabolite levels to efficiently utilize metabolic networks and avoid toxic buildup. In turn, metabolites dictate metabolic activity by acting as substrates, products, and effectors. Despite their foundational role in cell physiology, kinetics, and thermodynamics, absolute metabolite concentrations are seldom known. Here we develop an ensemble method for absolute metabolite quantitation and quantify 84 metabolites in T cells. Liquid chromatography-mass spectrometry of metabolites co-extracted from T cells and ^{13}C-labeled reference cells reveals absolute concentrations *en masse*. Across subtypes and individuals, T cell metabolomes resemble one another. T cells possess high adenylate energy charge and favorable redox ratios for energy and biomass production without compromising the forward driving force in glycolysis. Across metabolism, metabolite concentrations exceed their associated Michaelis constants and inhibitor constants two thirds and half of the time, respectively. The conserved features of T cell metabolomes underlie a design principle: metabolite levels prime cells for adaptive immune response.

Metabolism is a key driver of biological function and cellular proliferation[1]. Mounting evidence suggests that cellular metabolism in primary cells and *in vivo* is dissimilar to that of immortalized cells *in vitro*[2-5]. In addition to the mutations that cause cells to replicate indefinitely, disparate microenvironments shape their distinct metabolic states[6]. To better understand human metabolism, metabolite measurement from the cells, tissues, and blood of human subjects[7] and animal models[8-10] has been on the rise. While relative metabolite levels point to where in metabolic networks changes occur, they do not impart much knowledge of the functional implications of those changes. Absolute metabolite concentrations, on the other hand, provide mechanistic insights and foresights because they dictate reaction kinetics and thermodynamics as well as cell physiology (e.g., signaling and osmolarity). The physiological, kinetic, and thermodynamic significance warrants comprehensive absolute metabolite quantitation in primary cells and tissues.

Liquid chromatography-mass spectrometry (LC-MS) has been a workhorse in metabolomics[11]; however, matrix effects pose a challenge in converting ion currents to absolute concentrations[12]. To rectify them, cellular metabolites are spiked with known concentrations of internal standards. Stable isotopes are used to distinguish between intracellular metabolites and internal standards. For instance, internal standards containing naturally abundant isotopes (e.g., ^{12}C, ^{1}H, ^{16}O, etc.) are suitable for quantifying metabolite concentrations in cells that are grown on heavy isotope-labeled nutrients (e.g., ^{13}C, ^{2}H, ^{18}O, etc.) **(Fig. 1a)**. On the other hand, if cellular metabolites cannot be labeled with heavy isotopes, internal standards harboring heavy isotopes can be used with unlabeled cells[13] albeit costly and limited in scope due to low availability of isotopically labeled standards. In either case, known concentrations of internal standards and LC-MS measurement of labeled-to-unlabeled isotope ratios for individual metabolites reveal their absolute concentrations inside the cell[14]. The present isotope ratio-based approach, while effective for a handful of metabolites, becomes laborious, costly, and thus unscalable for comprehensive absolute metabolite quantitation.

The limited availability and proliferative capability of primary cells and *in vivo* samples further constrain absolute metabolite quantitation. The present isotope ratio-based method requires many rounds of metabolite extractions, thus correspondingly large amounts of biological materials, proportional to the number of metabolites to be quantified. Moreover, metabolites in non-proliferative cells are nearly impossible to fully label with heavy isotopes because they have slow turnover of macromolecules (e.g., proteins and nucleic acids) and biomass precursors (e.g., amino acids and nucleotides). The incomplete labeling obscures the distinction between cellular metabolites and internal standards, confounding the isotope ratio-based approach.

To address these challenges, we developed an ensemble metabolite quantitation method that leverages the known concentrations of >100 metabolites in previously quantified model systems including *E. coli* and immortalized mammalian cells[15] as internal reference. The reference cells were grown on uniformly ^{13}C-labeled glucose, [U-$^{13}C_6$] glucose, and co-extracted with human primary cells whose metabolite concentrations were unknown **(Fig. 1b)**. The known concentrations of the ensemble of metabolites in the reference cell and LC-MS measurement of labeled-to-unlabeled isotope ratios revealed absolute metabolite concentrations **(Fig. 1c)**.

Using the ensemble method, we quantified the absolute concentrations of 84 metabolites totaling 130-154 mM and 221 mM in human primary T cells and Jurkat T cells, respectively. Absolute metabolite

concentrations were conserved across subtypes and individuals. Amino acids were the largest class of metabolites in T cells with glutamate and aspartate being the most abundant metabolite in Jurkat cells and in primary T cells, respectively. The energy status of T cells was healthy with a high adenylate energy charge of 0.95 and favorable redox ratios $NADH/NAD^+$=~0.06 and $NADPH/NADP^+$= ~19. Thermodynamic analysis revealed that glycolysis and glutathione reductase were moderately to strongly forward driven with Gibbs free energy changes (ΔG) of –67 kJ/mol and –30 kJ/mol, respectively. Kinetic analysis revealed that T cell metabolomes promoted efficient enzyme utilization and regulation. Taken together, these findings pointed to a metabolic design principle: T cell metabolome is primed for energy generation, antioxidant activity, and efficiency. Our ensemble method is widely applicable to manifold primary cells and tissues to uncover the human metabolome and confer physiologically accurate insights into human metabolism.

Results

Co-extraction enables absolute metabolite quantitation *en masse*

Absolute metabolite concentrations offer quantitative insights into metabolic regulation, thermodynamics, and efficiency. We streamlined absolute metabolite quantitation by using isotopically labeled cellular metabolites as internal standards and co-extracting metabolites from the cells of interest (COI) and ^{13}C-labeled reference cells (REF). For each metabolite, ^{12}C-dominant peaks and ^{13}C-dominant ions were divided into unlabeled and labeled groups to account for impurities in the standard and natural ^{13}C abundance in the cells **(Fig. 1d)**. During co-extraction, two cell types were kept separate to prevent unwanted interactions and perturbations until they were quenched **(Fig. 1b)**. By using reference cells with known concentrations[15], the co-extraction method obviated the need for individual standards and parallelized absolute quantitation of multiple metabolites in a single sample.

To validate our approach, we performed co-extraction with known ratios of two cultures of *E. coli* grown on unlabeled or ^{13}C-labeled glucose in otherwise identical conditions **(Fig. 1e)**. LC-MS analysis revealed the ratios of unlabeled to ^{13}C-labeled metabolites (U:L ratio) as expected from the ratios of extracted culture volumes **(Fig. 1f)**. At all ratios tested (U:L ratio equal to 1:1, 4:1, and 20:1), the measurements globally stayed near the expected ratio with R^2=0.85, R^2=0.78, and R^2=0.67, respectively. However, the distributions of measured U:L ratios became broader as they deviated further from one due to the lower limit of detection and ion suppression in the mass spectrometer **(Extended Data Fig. 1)**. Since one-to-one ratios of unlabeled to ^{13}C-labeled metabolites minimized variance and error, we tuned the U:L ratios to be near one by extracting different amounts of the COI and the REF **(Fig. 1g)**. Measured U:L ratios depend on the intracellular aqueous volumes (V) and metabolite concentrations ([met]) in each cell type:

$$Measured\ U{:}L\ ratio = \frac{12C\ Ion\ Counts}{13C\ Ion\ Counts} = \frac{V_{COI} \times [met]_{COI}}{V_{REF} \times [met]_{REF}} \qquad \text{... Equation 1}$$

Starting from Eqn. 1, we solved for absolute metabolite concentrations in cells of interest using the known concentrations in the reference cell, aqueous cell volume ratios, and LC-MS measurement of unlabeled-to-labeled ion ratios.

Absolute metabolite quantitation in T cells by tailored co-extraction

We sought to comprehensively quantify absolute metabolite concentrations in human cells. Central carbon metabolites and most intermediates of amino acid and nucleotide biosynthesis pathways have turnover times ranging from a fraction of a second to minutes. Therefore, rapid quenching of metabolism and extraction of metabolites are required to minimize perturbation, accurately capture snapshots of metabolism, and quantify metabolites. Techniques for separating cells and tissues have been developed to minimize perturbations and facilitate metabolite extraction[16,17]. In the present work, we focused on quantifying absolute metabolite concentrations in human primary T cells.

We employed three quenching-extraction methods tailored to redox cofactors, metabolites present in the extracellular space (e.g., amino acids and pyruvate), and all others including central carbon metabolites **(Fig. 2a)**. Upon rapidly separating T cells in suspension by vacuum filtration, their metabolites were extracted with −20°C pre-cooled 40:40:20 acetonitrile/methanol/water and measured on LC-MS[17]. While our initial measurement was robust for many metabolites, redox cofactors were often undetectable, and amino acids were overestimated. For NAD(H) and NADP(H), we used an acidic extraction solvent, 0.1 M formic acid in 40:40:20 acetonitrile/methanol/water, followed by neutralization **(Fig. 2b** and **Extended Data Fig. 2a)**. Acidic extraction quenches residual enzymatic activity and dissociates metabolites by fully denaturing enzymes[13]. For amino acids, we found that vacuum pressure for filtration was an important variable. Pressure below −50 kPa expedited filtration, lowered amino acid levels belonging to extracellular space, and retained strictly intracellular metabolites such as nucleotides **(Extended Data Fig. 2b)**. However, amino acid signals under strong vacuum still reflected predominantly extracellular amino acids, calling for a wash step before metabolite extraction. Washing the cells and filter with ammonium acetate or PBS during the filtration step resulted in large decreases in both intracellular and extracellular metabolites, indicating cell shear and lysis **(Extended Data Fig. 2c)**. To rapidly remove extracellular metabolites and accurately measure their intracellular counterparts, we resorted to adding a centrifugation-and-wash step prior to vacuum filtration **(Fig. 2c)**. A single wash effectively removed extracellular amino acids **(Extended Data Fig. 2d)**. Our regular and acid extraction methods took a few seconds, and our amino acid extraction method incorporating the wash step took under three minutes. The fast extraction times left little time for metabolite levels to respond to any potential perturbations prior to quenching cellular activities. By combining the tailored co-extraction methods, we quantified the absolute concentrations of 68 metabolites totaling 221 mM in Jurkat cells **(Fig. 2d and Supplementary Table 1)**.

Cellular metabolome manifests genetic distance

Of the 221 mM measured metabolites in Jurkat cells, amino acids constituted the most abundant metabolite group, accounting for two thirds of known metabolome **(Fig. 2d)**. Of the remaining third (73 mM), central carbon metabolites, nucleotides, redox cofactors, and metabolites in degradation pathways made up 15%, 15%, 12%, and 18%, respectively. Glutamate was the most abundant metabolite at a concentration of 48 mM. Pyruvate and malate were the most abundant central carbon metabolites, and ATP and UTP were the most abundant nucleotides. Interestingly, 3-phosphoserine and uridine were two of the most abundant metabolites, pointing to the role of *de novo* serine[5] and pyrimidine[18] biosynthesis in T cell proliferation and development.

140 We compared the metabolome of Jurkat cells to those of other systems previously measured using the
141 traditional isotope ratio-based approach[15,19]. Metabolite concentrations were moderately correlated
142 between Jurkat cells and prokaryotic *E. coli* cells (R^2=0.43) **(Fig. 3a)**. Most amino acid concentrations were
143 higher in Jurkat cells, whereas the concentrations of select central carbon metabolites, nucleotides, and
144 redox cofactors were higher in *E. coli*. The Jurkat cell metabolome showed a higher correlation (R^2=0.48)
145 with eukaryotic *S. cerevisiae* cells than with *E. coli* **(Fig. 3b)**. Both microbes possessed greater
146 concentrations of glycolytic intermediates such as hexose phosphates, fructose-1,6-bisphosphate, and 3-
147 phosphoglycerate. Metabolite concentrations in Jurkat cells were highly correlated (R^2=0.64) with those of
148 another immortalized mammalian cell line (iBMK mouse kidney cells) **(Fig. 3c)**. The coefficients of
149 determination (R^2) indicated that 40-65% of the variance in metabolite concentrations in human T cells
150 could be accounted for by metabolite concentrations in other organisms. Regression analysis also revealed
151 that the metabolomes of eukaryotic and mammalian cells tended toward a closer resemblance. Thus, the
152 metabolome manifested evolutionary proximity of organisms.

153 **Conservation of T cell metabolome across subtypes and individuals**

154 Our ensemble method enabled absolute metabolite quantitation in human primary T cells from individual
155 healthy donors. To best capture *in vivo* T cell metabolism in two major T cell subtypes, we isolated CD4+
156 and CD8+ T cells by negative selection from peripheral blood mononuclear cells (PBMCs) because ligand
157 binding on cell surface may affect cellular metabolism[20]. To allow T cells to reach homeostasis, we
158 incubated them for two hours in RPMI 1640 medium supplemented with 10% dialyzed fetal bovine serum.
159 Within seven to nine hours of blood collection, we extracted CD4+ and CD8+ T cell metabolites using the
160 ensemble method **(Fig. 4a)**. The same-day measurement of T cell metabolome was chosen to minimize the
161 alteration of T cell proteome and study *in vivo*-like T cell metabolism before it adapted to *in vitro*
162 conditions.

163 We quantified 70 metabolites in CD4+ and CD8+ T cells from the five donors **(Fig. 4b and Supplementary**
164 **Tables 1 and 2)**. A total of 154 mM and 130 mM spanning central carbon metabolites, amino acids,
165 nucleotides, redox metabolites, and others was measured in CD4+ and CD8+ T cells, respectively.
166 Metabolomes of CD4+ and CD8+ T cells displayed a strikingly high correlation (R^2>0.95) **(Fig. 4c and**
167 **Extended Data Fig. 3a)**. Metabolite concentrations in CD4+ and CD8+ primary T cells also correlated with
168 those of immortalized Jurkat cells (R^2=0.88 and R^2=0.83). Amino acids represented the highest
169 concentration metabolite group (73% for CD4+ cells and 67% for CD8+ cells). The most abundant
170 metabolite measured in primary T cells was aspartate, unlike in Jurkat cells and other previously
171 characterized cell types, in which glutamate was the most abundant[15]. Across individuals, we observed
172 highly correlated T cell metabolomes (R^2>0.79) **(Fig. 4d and Extended Data Fig. 3b)**. The correlations
173 observed among primary T cell metabolomes exceeded those of T cell metabolomes compared with other
174 cell types (R^2=0.4-0.6) **(Extended Data Fig. 4)**. Thus, our observations pointed to the conservation of the T
175 cell metabolome among subtypes and individuals.

176 **Energetics of T cell metabolism revealed by absolute concentrations**

177 We sought to gain energetic and thermodynamic insights into T cell metabolism using absolute metabolite
178 concentrations. ATP is the cellular energy currency. Exergonic ATP hydrolysis drives reactions, which are
179 otherwise thermodynamically unfavorable, and produces ADP in the process. Thus, maintaining a high

180 ATP/ADP ratio favors proper cellular function. In both primary and immortalized T cells, ATP/ADP ratios
181 were consistently high with an interquartile range of 16.8–20.3 **(Fig. 5a)**, which is higher than those of
182 other eukaryotes yeast and iBMK cells (~3.95 and ~8.21, respectively)[15]. The high ATP/ADP ratio in
183 resting T cells may prime them for a rapid switch to proliferation and cytokine synthesis upon activation.
184 To fully account for cellular energetics, we quantified the adenylate energy charge, which reflects the total
185 energy stored in the adenylate pool.

186 $$Adenylate\ Energy\ Charge = \frac{[ATP] + {}^{1}/_{2}[ADP]}{[ATP] + [ADP] + [AMP]} \quad \text{... Equation 2}$$

187 The adenylate energy charge was 0.93-0.96, tightly conserved across all T cell types **(Fig. 5b)**. It was on the
188 higher end of the physiological range previously observed in mammalian cells (0.7 to 0.96)[15,21].

189 Oxidative phosphorylation is the main source of ATP for many organisms including humans. Using the
190 proton motive force due to electron transport from electron carriers such as NADH and $FADH_2$ to an
191 electron acceptor O_2, oxidative phosphorylation generates ATP. The $NADH/NAD^+$ ratio in T cells was
192 0.06±0.01 **(Fig. 5c)**. The ATP/ADP and $NADH/NAD^+$ ratios affect the thermodynamic driving force of
193 glycolysis, which generates two ATP and two NADH molecules for each glucose molecule **(Fig. 5d)**. We
194 determined the Gibbs free energy change (ΔG) across glycolysis to range from –60 kJ/mol to –77 kJ/mol
195 **(Fig. 5e and Supplementary Table 3)**. The majority (~75%) of Gibbs free energy drop occurred in upper
196 glycolysis **(Fig. 5f)**. Thus, the low $NADH/NAD^+$ ratio played dual roles of driving glycolysis forward (despite
197 the high ATP/ADP ratio) and preventing reactive oxygen species (ROS) production.

198 Redox pairs also play a vital role of providing reducing power for scavenging ROS and anabolism.
199 Glutathione and NADPH are primary reducing agents in the cell. We observed that T cells have the ratios of
200 antioxidant glutathione (GSH) to its oxidized counterpart glutathione disulfide (GSSG) to range from 4 to 12
201 **(Fig. 5g)**, which were in line with healthy erythrocytes which have GSH/GSSG=~5.88 (ref. [22]) but not as
202 high as those observed in human tissues[15,23] and whole blood[24]. For $NADPH/NADP^+$, we observed large
203 variations, but they were mostly high between 10 and 25 in T cells **(Fig. 5h)**. These values were consistent
204 with prior observations of $NADPH/NADP^+$ ratios of 2.30 in iBMK cells[15] and ~30 in immortalized mouse
205 embryonic fibroblasts[25]. In addition to benefiting anabolism, the high $NADPH/NADP^+$ ratio provided a
206 driving force for the glutathione reductase reaction with ΔG= –30±7 kJ/mol **(Fig. 5i)**. T cell energetics and
207 thermodynamics were conserved across all three T cell types.

208 **Efficient utilization and regulation of enzymes by T cells**

209 Metabolites serve as both substrates and effectors for enzymes. Enzyme-catalyzed reactions display
210 saturable kinetics with respect to metabolite concentrations, also known as Michaelis-Menten kinetics. As
211 the substrate and the effector increasingly occupy the active site and the effector binding site of an enzyme,
212 their influences on the reaction rate contract. Across all three T cell types, two thirds of substrate-enzyme
213 pairs displayed metabolite concentrations exceeding their corresponding Michaelis constants (K_m) **(Fig. 6a**
214 **and Supplementary Tables 4, 5 and 6)**. On the other hand, metabolites as inhibitors had their
215 concentrations exceed the corresponding dissociation constants of the enzyme-inhibitor complex (K_i) for
216 half of inhibitor binding interactions **(Fig. 6b and Supplementary Tables 7, 8 and 9)**. The distributions of
217 log ratios of metabolite concentrations to corresponding K_m values were similarly left-skewed, whereas log
218 ratios of metabolite concentrations to corresponding K_i values appeared more symmetrical **(Extended**

219 **Data Fig. 5)**. In each of the three T cell types, the former distribution of ln [met]/K_m leaned to the right
220 compared to the latter distribution of ln [met]/K_i **(Fig. 6c and Supplementary Table 10)**. On the
221 individual metabolite level, ATP and glutathione saturated the majority of enzyme binding sites as either
222 substrates or inhibitors, whereas cyclic AMP and $NADP^+$ hardly occupied enzyme binding sites **(Extended**
223 **Data Fig. 6)**. Non-saturating metabolites like cyclic AMP and $NADP^+$ may influence reaction rates through
224 mass action. On the other hand, saturating metabolites like ATP and glutathione would have to decrease
225 their concentrations drastically to influence reaction rates. Nonetheless, they may still influence reaction
226 rates by modulating ATP/ADP and GSH/GSSG ratios and shifting ΔG of near-equilibrium reactions[26,27]. The
227 concentrations of central carbon metabolites, amino acids, and nucleotides were distributed evenly around
228 the respective K_m and K_i values. Collectively, these observations manifested efficient utilization of enzymes
229 and modulation of enzyme activity by metabolite concentrations and reaction thermodynamics.

230 **Discussion**

231 The governing equations of biochemical systems mathematically describe, at the local level, the kinetics
232 and energetics of biochemical reactions, and at the systems level, the laws of conservation of mass and
233 energy. Absolute metabolite concentrations are integral elements of the governing equations. Since
234 analytical instruments have varying sensitivities and responses to disparate analytes, absolute metabolite
235 quantitation has remained an onerous task that requires large sample sizes. In particular, absolute
236 metabolite concentrations in primary cells and tissues have been inaccessible due to low availability of
237 biological materials. To solve this problem, we developed the ensemble method for quantifying absolute
238 metabolite concentrations *en masse*.

239 With our ensemble quantitation method in hand, we quantified absolute metabolite concentrations in
240 human T cells for the first time. T cell metabolism underlies adaptive immunity by supplying cellular
241 energy and biochemical building blocks for activation, differentiation, and proliferation[28-31] as well as
242 production of cytokines and cytotoxic granules[32-36]. Thus, knowledge of absolute concentrations provides a
243 quantitative and mechanistic understanding of T cell metabolism and establishes a solid foundation for
244 promoting immunity[37,38] and developing immunotherapy for cancer[20,39-41] and autoimmune diseases[42-45].

245 A key finding from our ensemble quantitation in human primary T cells is the conservation of metabolome
246 across subtypes and individuals. Between five individuals and their helper (CD4+) and killer (CD8+) T cells,
247 the lowest R^2 observed was 0.8. Despite helper and killer T cells carrying out distinct functions in the
248 adaptive immune system, their basal metabolic profiles resemble each other and indicate energy and redox
249 homeostasis. On the one hand, the high metabolic similarity across individuals implies that metabolic
250 variability may not stand in the way of allogeneic immunotherapy. On the other hand, ensemble absolute
251 metabolite quantitation across a larger number of individuals may reveal the unique metabolic features of
252 a "super donor," whose cells would lead to successful treatment of many patients. Thus, our data provides a
253 baseline for healthy T cell metabolism, opening the door to biomarker discovery.

254 The observed conservation of metabolite concentrations manifests a metabolic design principle: cells
255 prioritize concentration homeostasis despite a high turnover of metabolites. How can metabolites exert
256 control of metabolic activity without substantial change in concentrations? In reactions that are reversible
257 or moderately forward driven, small changes in metabolite concentrations lead to large changes in reaction
258 rates[26,46]. Furthermore, since each metabolite is involved in multiple reactions and pathways as substrates,

259 products and effectors, a substantial change in a single metabolite's concentration may have multiple
260 unintended consequences throughout metabolism[47]. Therefore, small variations across multiple
261 metabolites, rather than large variations of few metabolites, may better exercise precise pathway-level
262 modulation of metabolic activity. Caution should be taken, however, not to misconstrue the overall
263 similarity as lack of unique metabolic features.

264 The most notable difference between primary and immortalized T cells was the abundance of aspartate. In
265 primary T cells, aspartate is the most abundant metabolite at 35-39 mM, whereas in Jurkat cells it just
266 makes the top ten with 6.9 mM. Besides protein synthesis, aspartate serves three important functions: i)
267 electron translocation from the cytosol to the mitochondrial matrix as part of the malate-aspartate shuttle;
268 ii) biosynthesis of asparagine and nucleotides; and iii) anaplerosis. In T cells, both aspartate and asparagine
269 have been linked to stress response pathways and effector function. Aspartate deficiency is a biomarker of
270 autoimmune T cells from rheumatoid arthritis patients[42]. Aspartate deficiency lowers NAD^+/NADH and
271 ADP-ribosylation of GRP78/BiP, a regulator of endoplasmic reticulum (ER) stress, causing the expansion of
272 ER membrane and the biogenesis of a proinflammatory cytokine tumor necrosis factor (TNF). Aspartate
273 supplementation was sufficient to recover healthy T cell function. Furthermore, asparagine availability and
274 asparagine synthetase (ASNS) activity modulate T cell metabolism, effector function, and antitumor
275 response[48-50]. Thus, aspartate is a key regulator of T cell inflammatory response (*cf*. succinate and itaconate
276 in macrophages[51-53]) and we surmise that a high aspartate concentration is a hallmark of healthy T cells.

277 Besides uncovering the conserved features of T cell metabolism, a key contribution of this work is the
278 ensemble method for absolute metabolite quantitation, which standardizes metabolomics, augments its
279 utility and applicability, and engenders kinetic and thermodynamic insights. Knowledge of absolute
280 metabolite concentrations transcends the boundaries of individual metabolomics studies and lays the
281 foundation for cumulative knowledgebase of metabolism. Knowledge of absolute metabolite
282 concentrations is indispensable for quantifying fluxes in non-steady-state conditions[54,55]. The ensemble
283 method can be applied to not only suspension cultures but also adherent cell cultures and in *in vivo* tissue
284 extractions **(Extended Data Fig. 7)**. It would also facilitate organelle-specific metabolite quantitation[56],
285 uncover metabolite-protein interactions[57,58], and integrate multi-omic datasets[59]. We envision our
286 ensemble quantitation method being applied to the >400 major cell types in the human body[60] to create an
287 atlas of human metabolome. The resulting knowledge will serve as a conduit for connecting biochemistry
288 to mathematical modeling, advance model-based predictive biology, and reveal master regulators of
289 metabolism.

290 **Online Methods**

291 **Negative selection of CD4+ and CD8+ T cells**

292 CD4+ and CD8+ primary T cells were isolated from peripheral blood mononuclear cells (PBMCs) of healthy
293 donors by magnetic-activated cell sorting (MACS). PBMCs were isolated from healthy donor blood
294 (courtesy of the UCLA Blood and Platelet Center) by density gradient centrifugation using Ficoll-Paque
295 PLUS (Cytiva) (courtesy of the UCLA Virology Core Laboratory). To prevent unintended metabolic
296 reprogramming due to the binding of antibodies to the surface antigens of T cells[20,61], negative selection
297 strategies for CD4+ and CD8+ were employed. Manufacturer protocols for CD4+ and CD8+ negative
298 selection kits (Miltenyi Biotec) were followed. PBMCs were spun down, rinsed with PBS, and resuspended
299 in PBS containing 0.5% BSA and 2 mM EDTA (Miltenyi Biotec) at a concentration of 40 μL buffer per 10^7
300 cells. Then 10 μL of biotin-conjugated antibodies (Miltenyi Biotec) were added per 10^7 cells, and the cells
301 were incubated for 5 minutes in the refrigerator (2-8°C). After allowing antibodies to bind to cognate
302 antigens, 30 μL of buffer per 10^7 cells was added along with 20 μL of MicroBead Cocktail (Miltenyi Biotec)
303 per 10^7, and the cells were incubated for 10 minutes in the refrigerator (2-8°C). For negative selection of
304 CD4+ T cells, biotin-conjugated antibody cocktail included antibodies against CD8, CD14, CD15, CD16,
305 CD19, CD36, CD56, CD123, TCR γ/δ, and CD235a (Glycophorin A), and MicroBead Cocktail included
306 MicroBeads conjugated to anti-biotin antibody and anti-CD61 antibody to remove CD8+ T cells, monocytes,
307 neutrophils, eosinophils, B cells, dendritic cells, NK cells, granulocytes, γ/δ T cells, erythroid cells,
308 megakaryocytes, and platelets. For negative selection of CD8+ T cells, biotin-conjugated antibody cocktail
309 included antibodies against CD4, CD15, CD16, CD19, CD34, CD36, CD56, CD123, TCRγ/δ, and CD235a
310 (Glycophorin A), and MicroBead Cocktail included MicroBeads conjugated to anti-biotin antibody, anti-
311 CD14 antibody, and anti-CD61 antibody to remove CD4+ T cells, monocytes, neutrophils, eosinophils, B
312 cells, stem cells, dendritic cells, NK cells, granulocytes, γ/δ T cells, erythroid cells, megakaryocytes, and
313 platelets.

314 LS columns (Miltenyi Biotec) were rinsed with buffer, and then the cells were added to the columns. The
315 initial flow through represented the enriched CD4+ or CD8+ population. Once isolated, the cells were spun
316 down at 200g for 10 minutes, the supernatant was decanted, and the cells were resuspended in RPMI
317 supplemented with 10% dialyzed fetal bovine serum (dFBS). CD4+ or CD8+ T cells were cultured in an
318 incubator at 37°C for 1-2 hours before extraction. For amino acid measurement, cells from Donor E and
319 Donor F were cultured for two hours in standard RPMI 1640 media diluted threefold with amino acid
320 deprived RPMI media supplemented with 10% dFBS.

321 Population purity was verified with flow cytometry **(Extended Data Fig. 8)**. To confirm the purity of
322 isolated CD4+ and CD8+ T cells from PBMCs, cells were stained with the following antibodies: CD3 (APC,
323 clone REA613, Miltenyi Biotec), CD4 (VioBlue, clone REA623, Miltenyi Biotec), and CD8 (FITC, clone
324 REA715, Miltenyi Biotec). A suspension of 5×10^5 cells in 100 μL of PBS containing 0.5% BSA and 2 mM
325 EDTA was prepared. After 2 μL of each antibody solution was added, the cells were incubated on a shaker
326 at room temperature in the dark for 10 minutes, washed with 1 mL of buffer, centrifuged at 300g for 5
327 minutes, and resuspended to a volume of 0.5 mL of staining buffer. Samples were moved to a flow
328 cytometry tube and stored cold (2-8°C) in the dark until transport. Unstained and fluorescence minus one
329 (FMO) control samples were prepared similarly. Single color controls were prepared following the same

330 protocol with positive and negative compensation beads (Miltenyi Biotec) with the same concentration of
331 antibodies added (2 μL antibody solution per 100 μL PBS containing 0.5% BSA and 2 mM EDTA. Cells were
332 analyzed using an LSRFortessa flow cytometer (BD Biosciences), and data were gated and analyzed with
333 Floreada.io.

334 **Cell lines and culture conditions**

335 All cells were cultured in nutrient replete conditions. Jurkat cells (Jurkat clone E6-1, ATCC) were cultured
336 in RPMI 1640 (Gibco) supplemented with 10% dFBS at 37°C. For Jurkat cells, partial media change,
337 replacing one third of the cell-free culture volume, was performed every 24 hours and three hours prior to
338 metabolite extraction. Primary T cells were seeded into RPMI 1640 (Gibco) supplemented with 10% dFBS
339 at 37°C after negative selection, and their intracellular metabolites were extracted within one to two hours.
340 The cells designated for intracellular amino acid quantification and from Donor E were seeded into a
341 medium with one-third diluted amino acids but otherwise identical to RPMI 1640 supplemented with 10%
342 dFBS. *E. coli* strain NCM3722 was grown in Gutnick minimal medium[62] containing 2 g/L [U-$^{13}C_6$] glucose
343 and 10 mM NH_4Cl at 37°C. *E. coli* cells were cultured in the ^{13}C-labeled medium starting from the
344 inoculation of overnight cultures. Cells were reinoculated from the overnight culture into beveled flasks
345 and grown for four to five hours to the mid-exponential phase before metabolite extraction. *BAX*$^{-/-}$/*BAK*$^{-/-}$
346 immortalized Baby Mouse Kidney cells (iBMK)[63] cells were cultured in DMEM without glucose, pyruvate,
347 and glutamine (Gibco) supplemented with 4.5 g/L [U-$^{13}C_6$] glucose, 584 mg/L [U-$^{13}C_5$] glutamine (99%,
348 Cambridge Isotope Laboratories) and 10% dFBS in six-centimeter plates for 72 hours. Fresh medium was
349 replenished every 24 hours and three hours (2 g/L [U-$^{13}C_6$] glucose but otherwise the same medium) prior
350 to metabolite extraction.

351 **Co-extraction of metabolites from two cell types**

352 Jurkat, *E. coli*, and iBMK cells were all extracted when they were exponentially growing. Jurkat cells were
353 extracted when culture density was between 1×10^6 cells/mL to 3×10^6 cells/mL. *E. coli* cells were extracted
354 in the mid-exponential phase at OD_{600} between 0.3 and 0.6. iBMK cells were extracted when cultures
355 reached 60-80% confluence. Primary T cells were extracted one to two hours after isolation from PBMCs,
356 after incubating in RPMI 1640 + 10% dFBS. Viability and growth of mammalian cells were measured by
357 mixing cell suspension with Trypan Blue at a 1:1 ratio and using the Countess II FL Cell Counter (Thermo).

358 For co-extraction of T cells and *E. coli* cells, the two cultures were simultaneously vacuum filtered by
359 pipetting them onto distinct regions of a 47-mm nylon membrane (0.20-μm pore size). Care was taken to
360 ensure that the two cultures did not come in contact. Once the cells were separated from the media, the
361 filter was placed cell-side down onto a 6-cm plate containing 1 mL of pre-cooled (−20°C) 40:40:20 LC-MS
362 grade methanol/acetonitrile/water. Extraction continued in a −20°C freezer for 15-20 minutes. The filter
363 was flipped so that the cell side was facing up. The extract solution was mixed well, transferred to an
364 Eppendorf tube, and spun down at 17,000g and 4°C for 10 minutes. For measuring NAD(P)(H), an acidic
365 extraction solvent containing 0.1 M formic acid was used[64], and prior to centrifugation, the extract was
366 neutralized with 15% NH_4HCO_3. The supernatant was dried under nitrogen gas and reconstituted in LC-MS-
367 grade water for LC-MS analysis.

368 Measurement of intracellular amino acids in T cells required rapidly washing cells to minimize the
369 perturbation of cellular metabolism. Initially, two washing methods, in which 150 mM ammonium acetate
370 at a pH of 7.4 or PBS (Corning) was pipetted onto cells on nylon filter immediately after vacuum filtration,
371 were tested; however, both led to cell lysis and loss of metabolites. Instead, a combination of centrifugation
372 and vacuum filtration was used for rapid washing and extraction. T cells were first separated from media
373 by centrifuging 1 mL of culture at 500g for 2 minutes. The supernatant was removed and replaced with 1
374 mL of amino acid-free RPMI 1640 before rapid vacuum filtration and co-extraction as described above. For
375 Jurkat cells, which secreted substantial amounts of pyruvate, pyruvate measurement also followed rapid
376 washing and extraction steps as with amino acids.

377 For co-extraction of T cells and iBMK cells, both culture plates were removed from the incubator
378 simultaneously. Media was aspirated from the D3 plate, extraction solvent was placed on it, the plate was
379 placed on a cold plate. Jurkat cell culture was vacuum filtered on a nylon filter membrane, and the filter was
380 placed onto the iBMK extraction plate with the cell side facing down onto the extraction solvent **(Extended**
381 **Data Fig. 7a)**. The plate was placed in the –20°C freezer for 15-20 minutes. The adherent cells were
382 detached using a cell lifter, the filter was flipped cell-side up, and the extract solution was mixed well. The
383 metabolite extract was collected, spun down at 17,000g and 4°C for 10 minutes. The supernatant was dried
384 under nitrogen gas and reconstituted in LC-MS-grade water for LC-MS analysis.

385 **Metabolite measurement**

386 The metabolite extracts were analyzed by LC-MS, a Vanquish Duo UHPLC (Thermo) coupled to a Q Exactive
387 Plus mass spectrometer (Thermo). The LC separation was achieved using a hydrophilic interaction
388 chromatography column (XBridge BEH Amide Column, 130 Å, 2.5 µm, 2.1 mm × 150 mm, Waters). The A
389 and B solvents were 95:5 water/acetonitrile with 20 mM ammonium acetate, 39 mM ammonium hydroxide
390 (pH 9.4) and 99:1 acetonitrile/water, and the gradient was the same as previously reported[20,65]. MS was
391 performed in positive and negative ion mode with a mass resolution of 140,000 at 200 *m/z* (mass-to-
392 charge ratios). LC-MS data were processed using the Metabolomic Analysis and Visualization Engine
393 (MAVEN)[66]. The m/z values from monoisotopic masses and the retention times from authenticated
394 standards were used to identify peaks. For isomers glucose-6-phosphate and fructose-6-phosphate, which
395 were not separated by the LC method, the ratio of isomers in the cells of interest was assumed to be the
396 same as in the reference cells, and a single peak and U/L ratio were taken for both isomers. For arginine
397 and glycine, whose concentrations could not be reliably obtained from co-extraction, known concentrations
398 of arginine and glycine standards were spiked into cellular extracts, and cellular arginine and glycine
399 concentrations were computed using the increase in the ion counts relative to the unspiked aliquots and
400 the ion counts in the unspiked aliquots. A previously reported concentration value for dTTP concentration
401 in *E. coli* was inaccurate. To measure the correct absolute concentration of dTTP in *E. coli*, *E. coli* strain
402 NCM3722 was grown in Gutnick minimal medium[62] containing 2 g/L [U-$^{13}C_6$] glucose and 10 mM NH_4Cl at
403 37°C , and metabolites were extracted using 40:40:20 methanol/acetonitrile/water containing a known
404 amount of unlabeled dTTP. The samples were prepared and analyzed as described above, and the new
405 dTTP concentration was calculated from the ratio of unlabeled to labeled dTTP. The new dTTP
406 concentration in *E. coli* was 1.81×10^{-4} M with the 95% confidence interval [1.54×10^{-4} M, 2.13×10^{-4} M]. Using
407 this new reference concentration, dTTP concentrations in T cells were determined using the co-extraction
408 method.

409 **Absolute metabolite quantitation and statistical analysis**

410 Absolute metabolite concentrations were determined by the ratio of unlabeled to ^{13}C-labeled metabolites,
411 the ratio between aqueous cell volumes of cells of interest and reference cells, and the known absolute
412 concentration in the reference cells. The concentration of each metabolite was calculated by:

413 $$\ln[met]_{COI} = \ln\frac{U}{L} + \ln\frac{V_{REF}}{V_{COI}} + \ln[met]_{REF} \qquad \text{... Equation 3}$$

414 Where $[met]_{COI}$ and $[met]_{REF}$ is the metabolite concentration in the cells of interest (COI) and reference
415 cells (REF) , $\frac{U}{L}$ is the ratio of unlabeled ions to labeled ions, V_{COI} and V_{REF} are the aqueous cell volumes of
416 COI and REF. For *E. coli*, culture density (OD_{600}) was measured using a spectrophotometer and converted to
417 aqueous cell volume using the conversion[15] $1\ OD_{600} = \frac{7\times10^{-16}\ L\ (aqueous\ vol)}{1\ cell}\frac{1\ cell}{3\times10^{-13}\ gCDW}\frac{0.47\ gCDW}{1\ L\ (culture)}$. For
418 primary T cells, Jurkat cells, and iBMK cells, packed cell volume was measured and converted to the
419 aqueous cell volume using the conversion $1\ \mu L\ (PCV) = 0.7\ \mu L\ (aq\ vol)$.

420 Once metabolites concentrations were determined using **Eqn. 3** for individual samples, average levels and
421 confidence intervals for metabolites were derived by bootstrapping. Since $\frac{U}{L}$ values influenced the accuracy
422 of metabolite concentration measurement **(Fig. 1f)**, bootstrapping was carried out by weighting metabolite
423 concentrations based on $\frac{U}{L}$. The weights were derived from the relationship between $\frac{U}{L}$ and the
424 corresponding R^2 values across the metabolome in the co-extraction validation study **(Fig. 1f)**.

425 $$R^2(k) = 1 - \frac{SS_{res}}{SS_{tot}} = 1 - \frac{\sum_i(\log U_i - \log kL_i)^2}{\sum_i(\log U_i - \overline{\log U})^2} \qquad \text{... Equation 4}$$

426 k represents expected $\frac{U}{L}$ ratio (1, 4, and 20 in the validation study), i represents metabolite index, and U_i
427 and L_i represent ion counts for unlabeled and ^{13}C-labeled metabolite i.

428 The weights for individual metabolite concentrations in bootstrapping were determined by the likelihood
429 of the measurements given their $\frac{U}{L}$ values accurately capturing the true concentrations, which were
430 represented by R^2. To determine weights for the individual samples whose metabolites were extracted
431 from various $\frac{U}{L}$ values, the known k and R^2 values were fitted to a gaussian curve using nonlinear regression
432 **(Extended Data Fig. 9)**. The resulting weight function $w\left(\frac{U}{L}\right)$ was used to determine probabilities for
433 weighted bootstrapping of T cells concentrations measurements.

434 $$w\left(\frac{U}{L}\right) = a \times e^{-\frac{\left(\ln\frac{U}{L}\right)^2}{2c^2}} \qquad \text{... Equation 5}$$

435 The values a = 0.831451 and c = 4.575862 were determined by non-linear least squares fitting. Each $\frac{U}{L}$ ratio
436 was converted to a weight value w_i using **Eqn. 5**. For each metabolite, the probability of selecting a
437 measurement in weighted bootstrapping was computed by dividing its weight by the sum of the weights of
438 all measurements:

439 $$P(i) = \frac{w_i}{\sum_j w_j} \qquad \text{... Equation 6}$$

440 For each metabolite, the log-concentration ($\ln[met]_{COI}$) distribution was bootstrapped by resampling
441 10,000 means, each of which was calculated from n (number of samples) log-concentration measurements
442 selected according to $P(i)$ with replacement **(Extended Data Fig. 9)**. The standard error s_{met} of log-
443 concentrations from the bootstrapped distribution was obtained by dividing the range of the 95%
444 confidence interval by 4. However, this error represented a compounding effect of independent random
445 errors from both COI (T cells) and REF cells. The errors for metabolites specifically in COI (T cells) were
446 propagated using the compound standard error s_{met} and the standard error of $[met]_{REF}$ ($s_{[met]_{REF}}$):

447 $$s_{[met]_{COI}} = \begin{cases} \sqrt{{s_{met}}^2 - {s_{[met]_{REF}}}^2} & {s_{met}}^2 > {s_{[met]_{REF}}}^2 \\ s_{[met]_{REF}} & {s_{met}}^2 \leq {s_{[met]_{REF}}}^2 \end{cases} \quad \text{... Equation 7}$$

448 The 95% confidence interval of each metabolite was determined as the mean ± 2 $s_{[met]_{COI}}$ in logarithmic
449 space:

450 $$\ln[met]_{COI} \in [\overline{\ln[met]_{COI}} - 2s_{[met]_{COI}}, \overline{\ln[met]_{COI}} + 2s_{[met]_{COI}}] \quad \text{... Equation 8}$$

451 **Michaelis constants (K_m) and inhibitor dissociation constants (K_i)**

452 Absolute metabolite concentrations were compared to previously published Michaelis constants (K_m) and
453 inhibitor dissociation constants (K_i). K_m and K_i values in *Homo sapiens* were extracted from BRENDA using
454 the Python 3 implementation of the Simple Object Access Protocol (SOAPpy)[67]. Entries corresponding to
455 mutant enzymes were removed. When multiple entries for the same enzyme-metabolite pair were
456 available, K_m or K_i was represented by the geometric mean. The ln([met]/K_m) and ln([met]/K_i)
457 distributions were compared using the Kolmogorov-Smirnov test. The skewness of each distribution was
458 represented by the Fisher-Pearson coefficient of skewness (g_1).

459 **Gibbs free energy of reaction**

460 Gibbs free energies of lumped glycolytic steps and glutathione reductase were calculated using the
461 eQuilibrator API[68] by inputting the measured absolute concentrations of glycolytic intermediates, ATP,
462 ADP, inorganic phosphate, NAD(H), NADP(H), glutathione, and glutathione disulfide. Inorganic phosphate
463 concentration was set to the geometric mean of the range 2.5-5 mM based on the phosphate concentration
464 in RPMI 1640 of 5.6 mM (Gibco) and previous measurements in mammalian cells[69,70]. Intracellular glucose
465 concentration was set to the geometric mean of the range 0.1-6 mM based on previous measurements in
466 mammalian cells[71-73]. For intracellular inorganic phosphate and glucose, the standard errors of their log-
467 concentrations were obtained by dividing the reported range in logarithmic space by 4.

468 Gibbs free energy changes for lumped reactions were calculated when intermediate metabolite
469 concentrations were unknown. Gibbs free energy changes for the following reactions and lumped reactions
470 were calculated.

471 Hexokinase (HK) reaction:

472 $$Glucose + ATP \rightarrow G6P + ADP$$

473 Phosphoglucoisomerase (PGI) reaction:

$$G6P \rightarrow F6P$$

Phosphofructokinase (PFK) reaction:

$$F6P + ATP \rightarrow FBP + ADP$$

Lumped fructose-bisphosphate aldolase (FBA), triosephosphate isomerase (TPI), glyceraldehyde-3-phosphate dehydrogenase (GAPDH), phosphoglycerate kinase (PGK) reactions:

$$FBP + 2\,NAD + 2\,Pi + 2\,ADP \rightarrow 2\,3PG + 2\,NADH + 2\,ATP$$

Lumped phosphoglycerate mutase (PGAM), enolase (ENO) reactions:

$$3PG \rightarrow PEP + H_2O$$

Pyruvate kinase (PYK) reaction:

$$PEP + ADP \rightarrow PYR + ATP$$

Overall glycolysis:

$$Glucose + 2\,NAD + 2\,ADP + 2\,Pi \rightarrow 2\,PYR + 2\,NADH + 2\,ATP + 2\,H_2O$$

Glutathione reductase:

$$NADPH + GSSG + H^+ \rightarrow NADP^+ + 2\,GSH$$

The error for each reaction step was calculated by error propagation with the standard errors of the standard Gibbs free energy and the log-concentrations of substrates and products **(Supplementary Table 3)**. For instance, the error propagation formula for the Gibbs free energy of a reaction with the form $aA + bB \rightarrow cC + dD$, where lowercase letters represent stoichiometric coefficients for metabolites in capital letters was:

$$s_{\Delta G} = \sqrt{(s_{\Delta G^\circ})^2 + (RT)^2((a \cdot s_{ln[A]})^2 + (b \cdot s_{ln[B]})^2 + (c \cdot s_{ln[C]})^2 + (d \cdot s_{ln[D]})^2)} \quad \text{... Equation 9}$$

497 **Data availability**

498 Source data for all Figures (absolute metabolite concentrations, kinetic constants, and thermodynamic
499 constants) are provided in Supplementary Tables 1-10 and the GitHub public repository:
500 https://github.com/samokeeffe/abs-met-quant

501 **Code availability**

502 The code for bootstrapping and computational analyses is available on the GitHub public repository:
503 https://github.com/samokeeffe/abs-met-quant

504

505 **Acknowledgements**

506 The authors would like to thank the members of the Park lab, the UCLA Molecular Instrumentation Center,
507 the UCLA Metabolomics Center, the UCLA-CDU Center for AIDS Research (CFAR), and the UCLA Flow
508 Cytometry Core for helpful discussion. PBMCs were obtained from the UCLA-CDU CFAR Virology Core Lab
509 that is supported by National Institutes of Health grant number 5P30 AI028697. Flow cytometry was
510 performed in the UCLA Jonsson Comprehensive Cancer Center (JCCC) and Center for AIDS Research Flow
511 Cytometry Core Facility that is supported by National Institutes of Health awards P30 CA016042 and 5P30
512 AI028697 and by the JCCC, the UCLA AIDS Institute, the David Geffen School of Medicine at UCLA, the UCLA
513 Chancellor's Office, and the UCLA Vice Chancellor's Office of Research. This work was supported by the
514 National Institutes of Health under instrumentation grant number 1S10OD016387-01, the National Center
515 for Complementary and Integrative Health of the National Institutes of Health under award number
516 R21AT012814 (J.O.P.), and the National Institute of General Medical Sciences of the National Institutes of
517 Health under award number R35GM143127 (J.O.P.).

518

519 **Contributions**

520 S.O.K. and J.O.P. designed the study and wrote the manuscript. S.O.K., H.S., E.M., and J.O.P. carried out the
521 experiments. S.O.K. and H.S. isolated primary T cells and performed flowcytometry. S.O.K., H.S., E.M. and
522 J.O.P. performed metabolomics analysis.

Figures

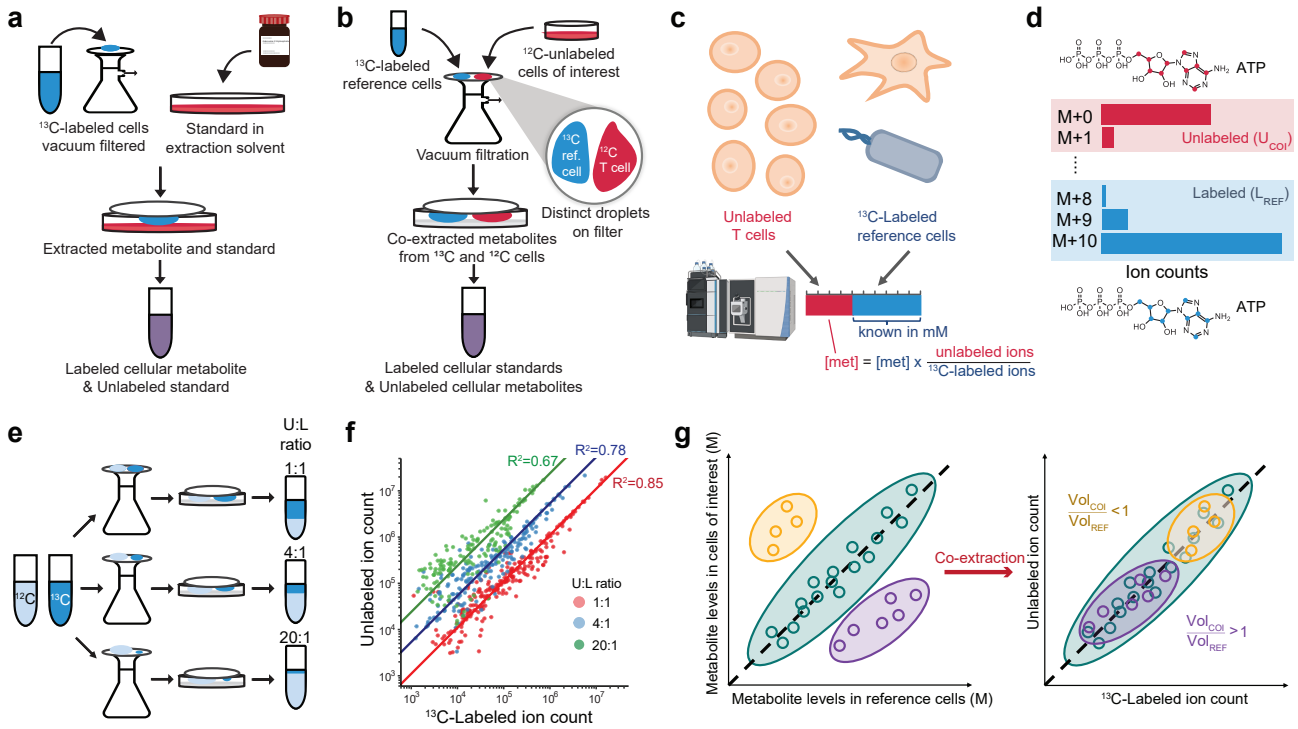

Figure 1. Metabolite co-extraction enables ensemble quantitation using ^{13}C-labeled metabolome as an internal standard. (**a**) Traditional absolute metabolite quantitation relies on the use of an authenticated standard dissolved in metabolite extraction solvent. Cells of interest are grown in ^{13}C-labeled media and extracted into the solvent containing the known concentration of the unlabeled standard. (**b**) Simultaneous extraction of metabolites from two cell types, one of which was ^{13}C-labeled, allowed absolute quantitation of multiple metabolites in parallel. Care was taken to not put the two cell types in contact during co-extraction. (**c**) The resulting LC-MS peaks contained a mixture of unlabeled metabolites from T cells (or other cells of interest) and ^{13}C-labeled metabolites from reference cells. Using the ratios of unlabeled to labeled metabolite peaks and the known concentrations of metabolites in reference cells (blue), absolute metabolite concentrations in T cells were obtained. (**d**) For each metabolite that has n carbons, multiple mass isotopomers with monoisotopic masses from M+0 (unlabeled) to M+n (fully ^{13}C-labeled) were observed. Considering natural ^{13}C abundance, isotope impurity, and $^{12}CO_2$ incorporation metabolic pathways, each mass isotopomer was attributed to either the cell of interest (COI) or the reference cell (REF). (**e**) The ensemble quantitation method was tested by co-extracting unlabeled and ^{13}C-labeled *E. coli* at the ratios of 1:1, 4:1 and 20:1. (**f**) The accuracy of the method was validated by plotting the unlabeled ion counts and labeled ion counts for individual metabolites and comparing them to the expected U:L ratios (n = 3 biological replicates for each ratio). The R^2 values were computed with respect to the expected ratio lines. (**g**) Cell density and extraction volumes were tuned to achieve U:L ratios near 1:1 to minimize measurement errors.

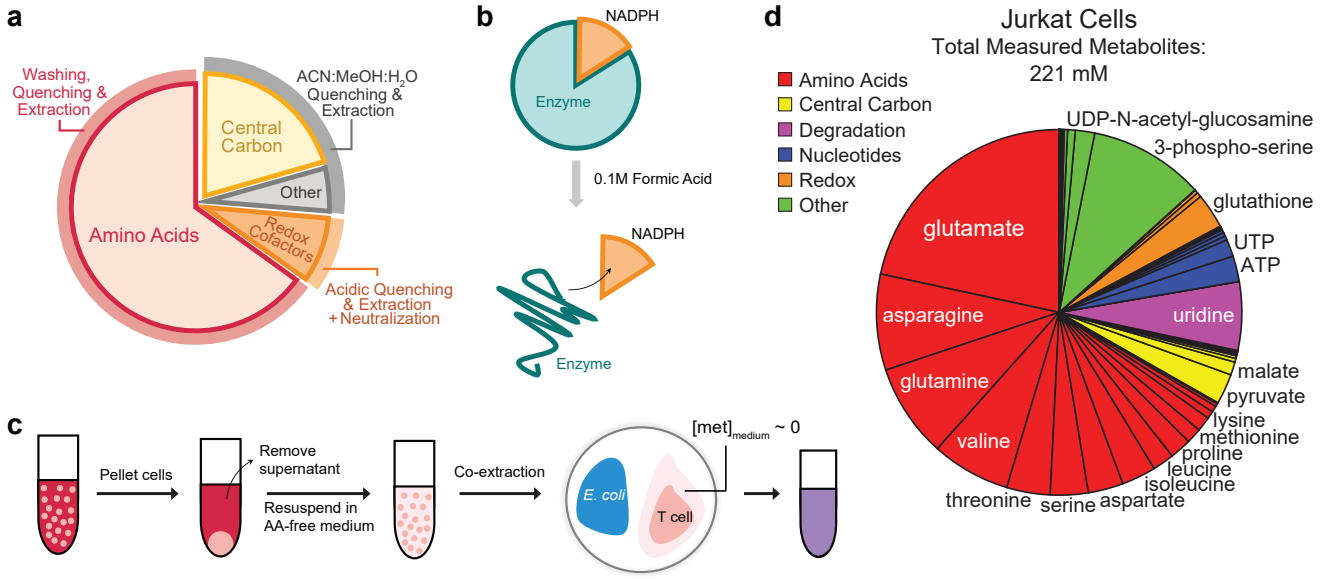

Figure 2. Tailored co-extraction techniques reveal T cell metabolome. (**a**) Three methods for quenching metabolism and extracting metabolite, which were tailored to different metabolite classes, enabled comprehensive metabolite quantitation. (**b**) To extract and measure NAD(P)H, an acidic extraction solvent containing 0.1M formic acid was used to denature enzymes and dissociate them. Acidic extracts were neutralized to prevent the degradation of metabolites. (**c**) To measure intracellular amino acids without interference from extracellular amino acids, cells were pelleted, supernatant was quickly removed, and amino acid-free medium was provided prior to co-extraction. (**d**) The three co-extractions methods revealed the metabolome of Jurkat cells in absolute units.

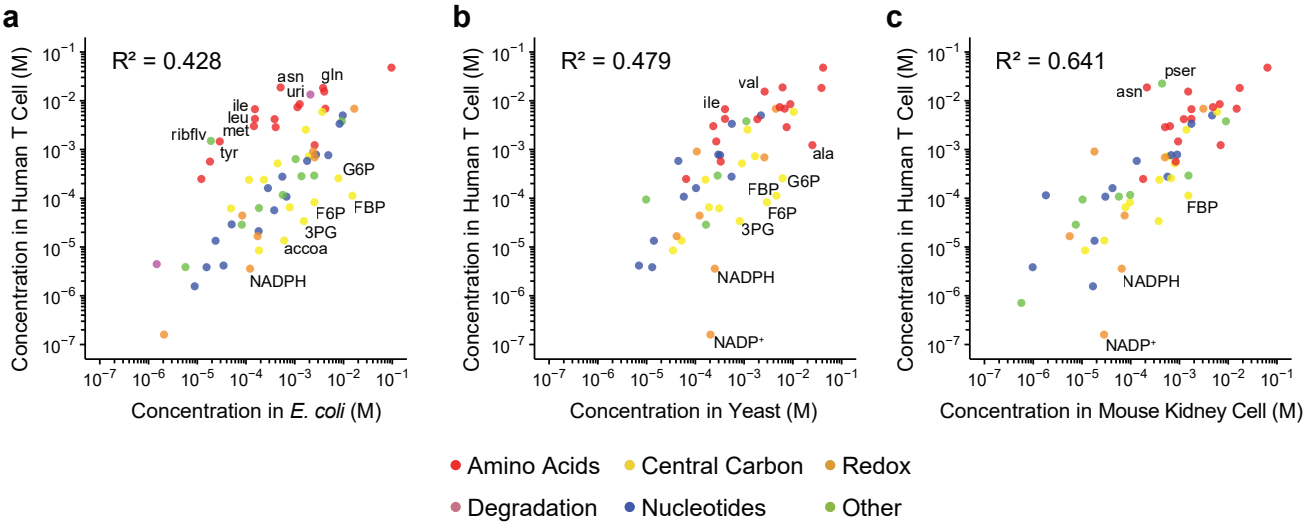

Figure 3. Comparison of metabolomes between divergent organisms. (**a**) Absolute metabolite concentrations in Jurkat cells and *E. coli* cells are compared. (**b**) Absolute metabolite concentrations in Jurkat cells and yeast cells are compared. (**c**) Absolute metabolite concentrations in Jurkat cells and immortalized baby mouse kidney (iBMK) cells are compared. G6P denotes glucose-6-phosphate; F6P, fructose-6-phosphate; FBP, fructose-1,6-bisphosphate; 3PG, 3-phosphoglycerate; pser, phosphoserine; ribflv, riboflavin; uri, uridine; and accoa, acetyl-CoA.

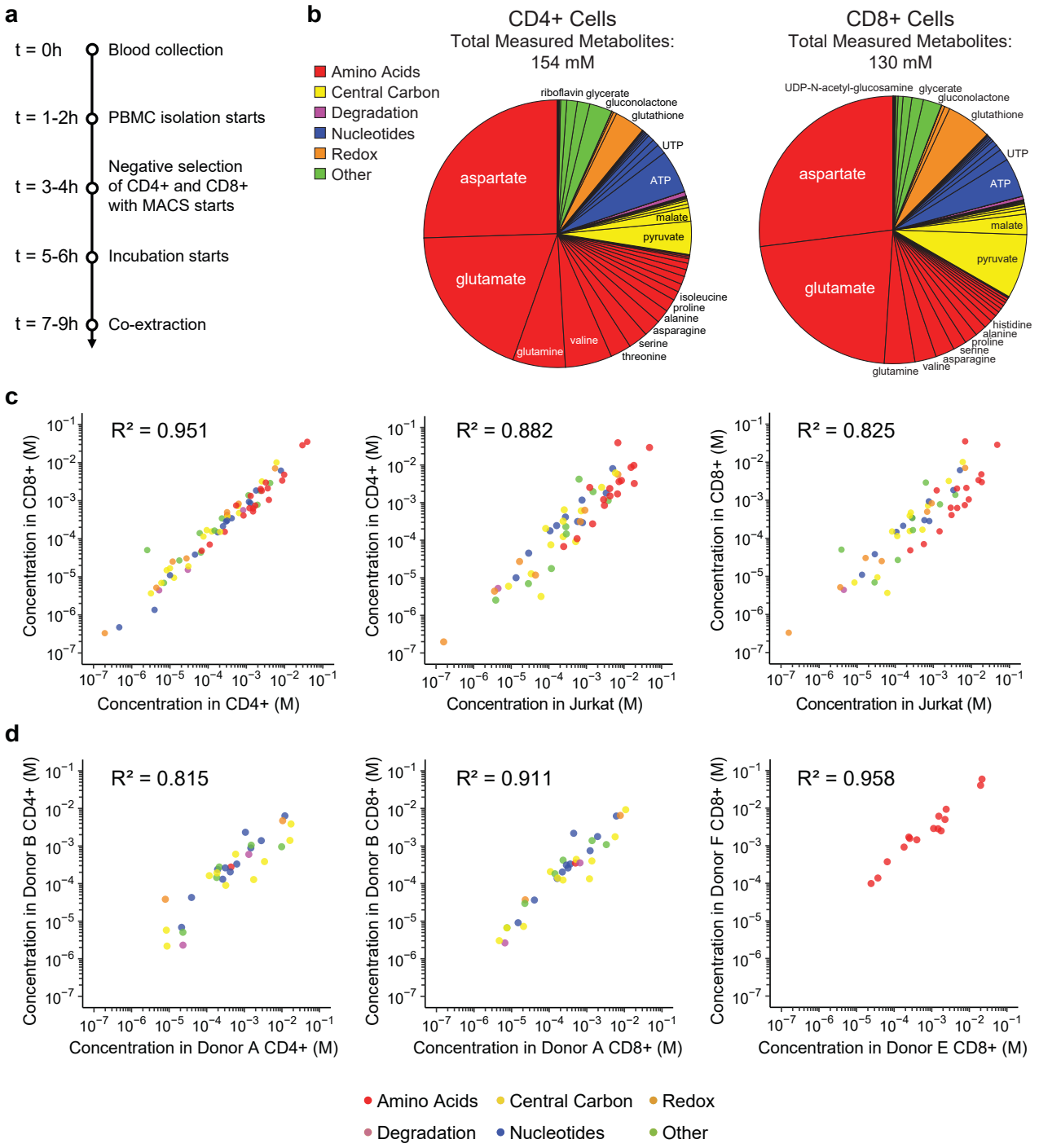

Figure 4. Conservation of metabolite concentrations in human primary T cells across subtypes and individuals. (**a**) Primary cell metabolites were quenched and extracted within 7–9 hours of blood collection from healthy donors. (**b**) Absolute metabolite concentrations were quantified in CD4+ helper T cells and CD8+ killer T cells derived from five donors. (**c**) Absolute metabolite concentrations were compared between primary CD4+ and CD8+ T cells and between primary and Jurkat T cells. (**d**) Absolute metabolite concentrations were compared between different donors for each subtype.

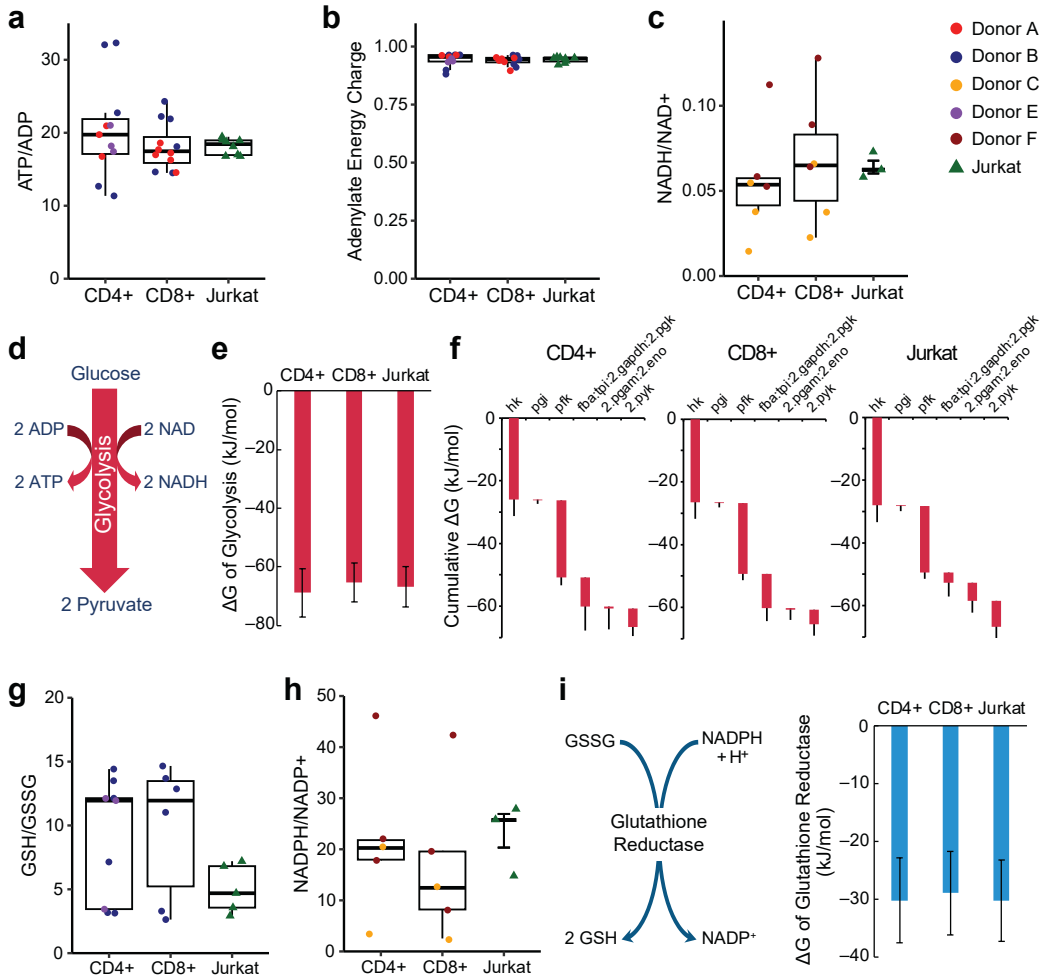

Figure 5. Energetics of T cell metabolism. (**a**) The ratio of ATP to ADP concentrations were calculated for primary CD4+ and CD8+ T cells and Jurkat cells (n = 12 replicates derived from three and two donors for CD4+ and CD8+ T cells, respectively; n = 8 replicates for Jurkat cells). (**b**) The adenylate energy charge was calculated using the concentrations of ATP, ADP, and AMP (n = 12 replicates derived from three and two donors for CD4+ and CD8+, respectively; n = 8 replicates for Jurkat cells). (**c**) The ratio of reduced NADH to oxidized NAD^+ was calculated (n = 6 replicates derived from two donors for CD4+ and CD8+ T cells; n = 3 replicates for Jurkat cells). (**d**) Glycolysis converts each molecule of glucose into two molecules of pyruvate while generating two ATP and two NADH. (**e**) Overall Gibbs free energy change across glycolysis in T cells was computed using the net reaction of glycolysis. (**f**) Using the absolute concentrations of glycolytic intermediates, stepwise and cumulative Gibbs free energy changes across glycolysis were computed. (**g**) The ratio of reduced glutathione to oxidized glutathione disulfide was calculated (n = 9 replicates derived from two donors for CD4+ T cells; n = 6 replicates derived from a single donor for CD8+ T cells; n = 5 replicates for Jurkat cells). (**h**) The ratio of reduced NADPH to oxidized $NADP^+$ was calculated (n = 5 replicates derived from two donors for CD4+ and CD8+ T cells; n = 3 replicates for Jurkat cells). (**i**) Glutathione reductase generates reduced glutathione using the reducing power of NADPH. Glutathione reductase was strongly forward driven across all T cell types. Error bars represent the 95% confidence intervals. Boxplots show boxes that extend from the first to third quartile with thick lines representing the median. The whiskers extend to the farthest measurement values within 1.5 times the interquartile range from the edges of the box.

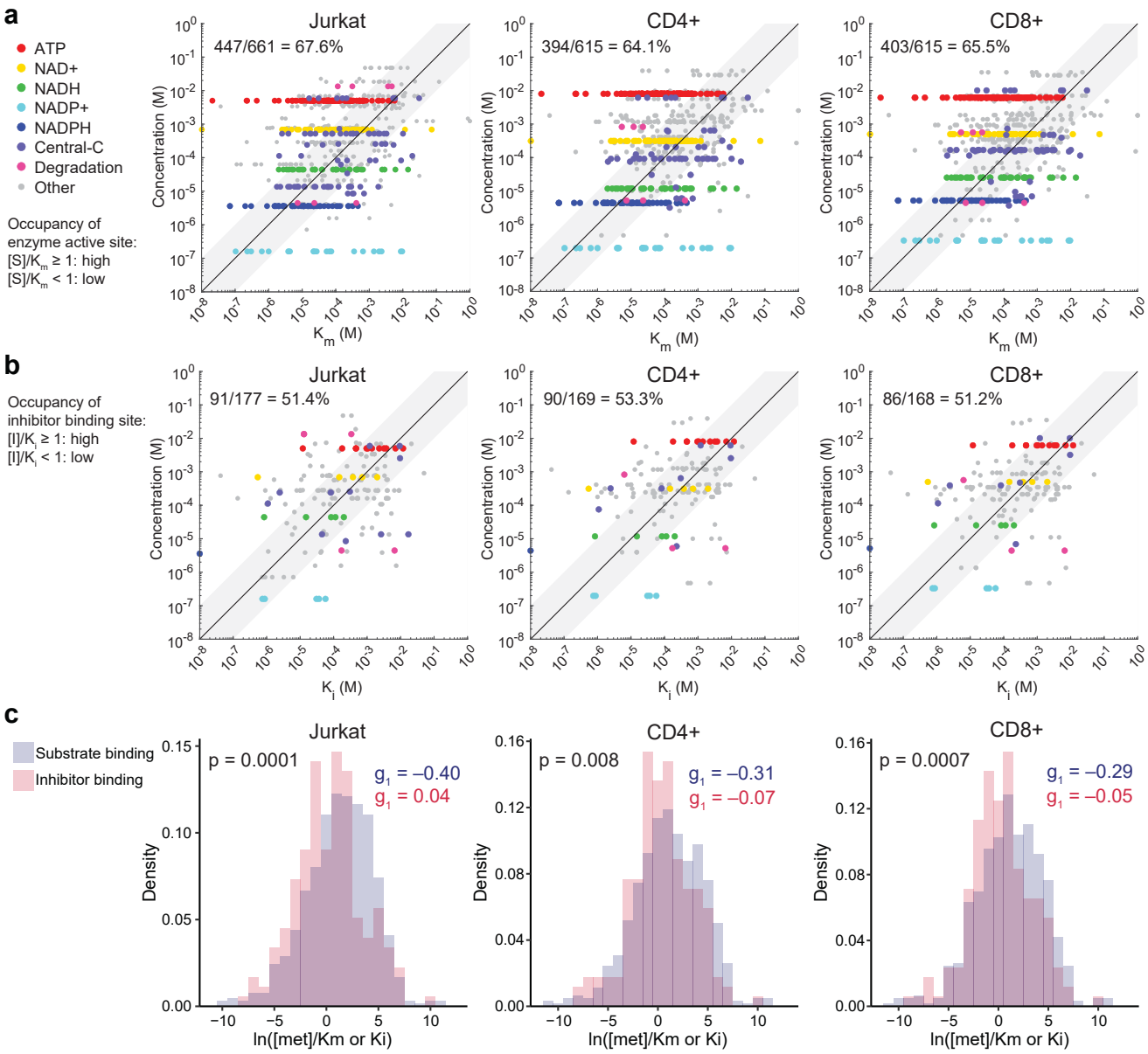

Figure 6. Comparison of metabolite concentrations to Michaelis constants (K_m) and inhibitor dissociation constants (K_i). (**a**) Absolute metabolite concentrations were compared with the K_m values for the associated enzyme active sites. The fraction of concentrations exceeding K_m is shown. (**b**) Absolute metabolite concentrations were compared with the K_i values for the associated inhibitor binding sites. The fraction of concentrations exceeding K_i is shown. (**c**) Tendencies for substrate-enzyme binding and inhibitor-enzyme binding were compared across T cell types. P values were computed from the Kolmogorov-Smirnov test comparing the two distributions of $\ln([met]/K_m)$ and $\ln([met]/K_i)$. g_1 values represent the Fisher-Pearson moment coefficient of skewness.

597 **Extended Data Figures**

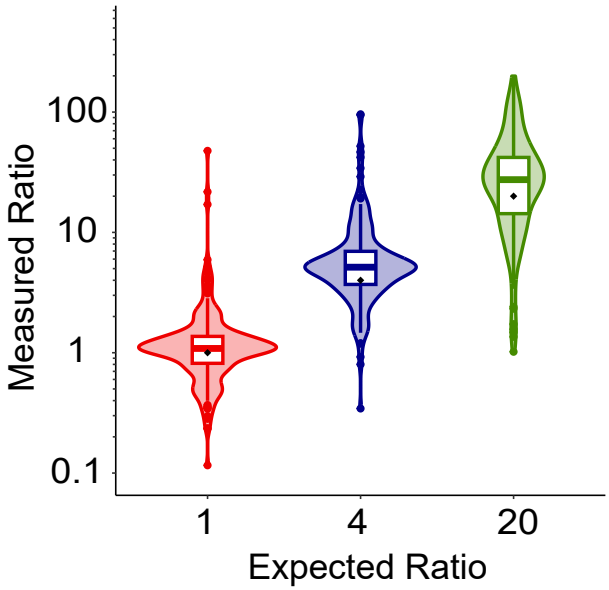

598

599 **Extended Data Figure 1. Validation of metabolite co-extraction for ensemble quantitation.**
600 Distributions of measured ratios of unlabeled (^{12}C) to ^{13}C-labeled metabolites from unlabeled and labeled *E.*
601 *coli* cultures co-extracted at the ratios of 1:1, 4:1 and 20:1. The black diamonds represent the expected
602 ratios 1, 4, and 20.

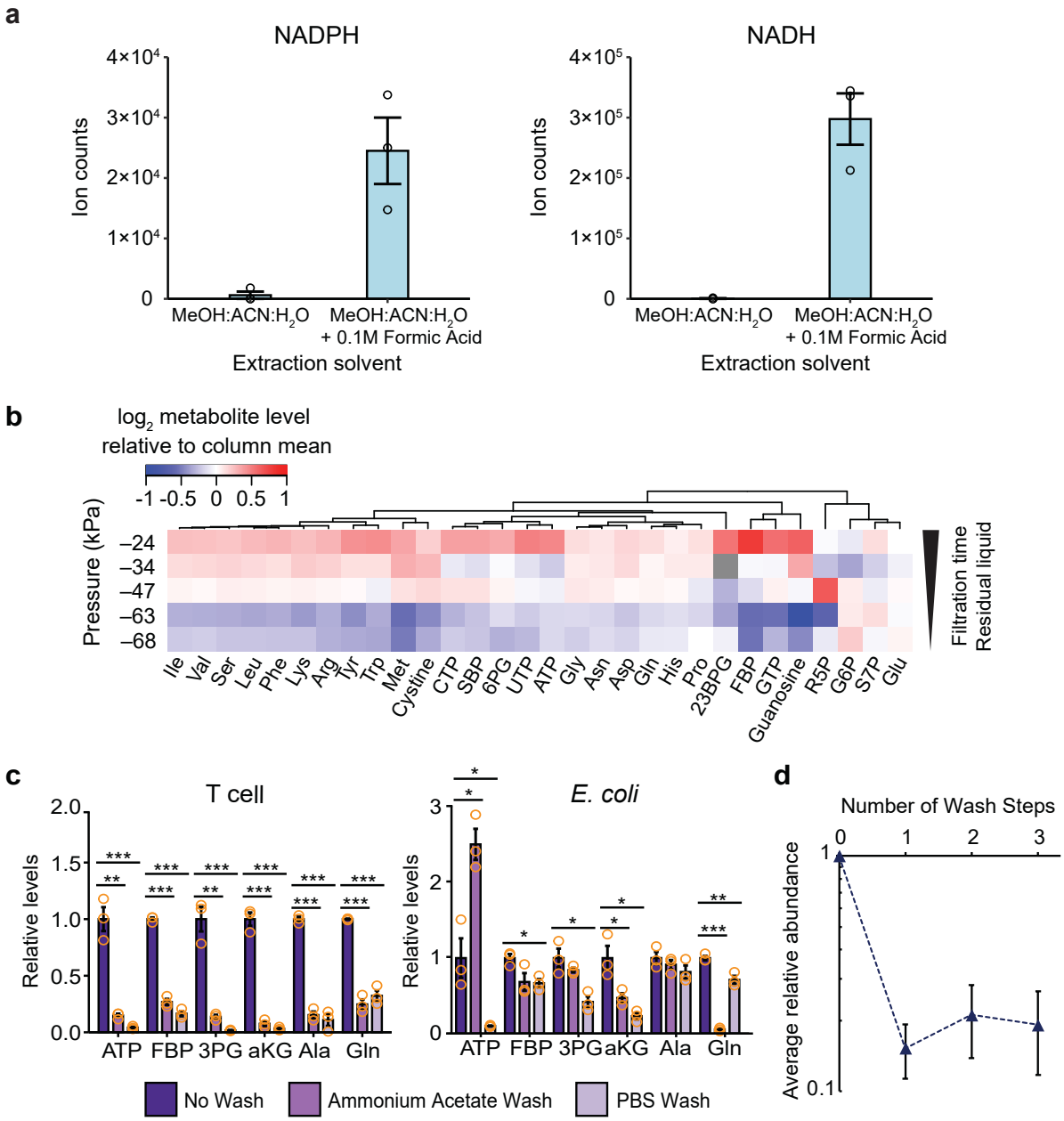

Extended Data Figure 2. Tailored metabolite extraction methods for comprehensive quantitation. (**a**) Acidic quenching increased ion counts for NADPH and NADH. Error bars represent the s.e.m. (n = 3 biological replicates). (**b**) Relative metabolite abundances were measured after extracting T cells at different vacuum pressures. The averages of n = 3 biological replicates were column mean centered. (**c**) Relative abundances of representative metabolites were measured with and without washing cells. Either 150 mM ammonium acetate (pH 7.4) or PBS was used for washing T cells and *E. coli*. Error bars represent the s.e.m. (n = 3 replicates). P values were calculated using two-tailed t-tests (* represents $p \leq 0.05$, ** represents $p \leq 0.01$, *** represents $p \leq 0.001$). (**d**) Amino acids were measured after wash steps and compared to the measurement with no wash. The averages of relative amino acid levels are shown with error bars representing the s.e.m. (n = 14 amino acids). A single centrifuge and wash step was sufficient to eliminate the interference from extracellular amino acids.

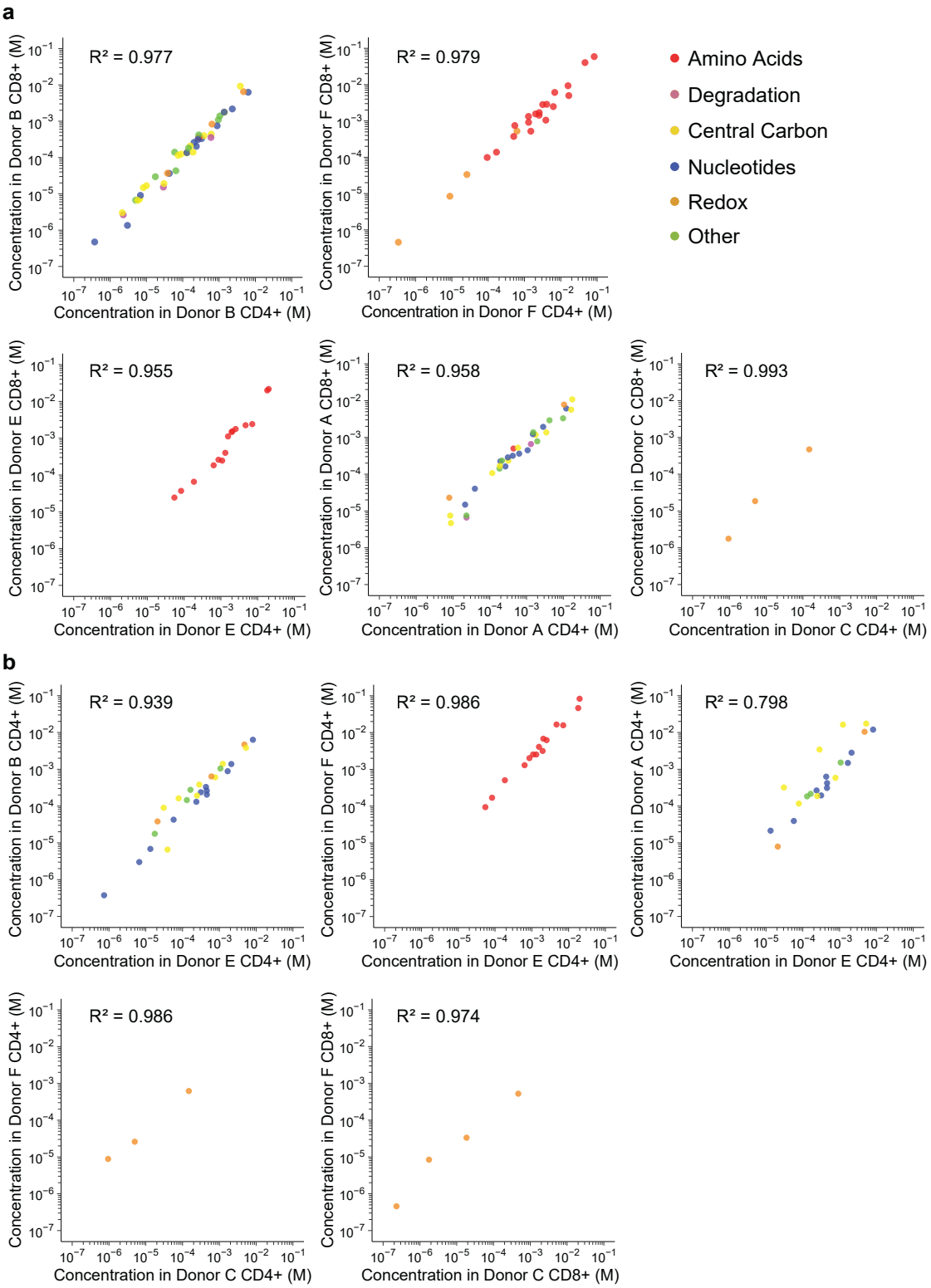

Extended Data Figure 3. Comparison of T cell metabolomes across subtypes and individuals. (**a**) Absolute metabolite concentrations were compared between CD4+ and CD8+ T cells for each donor. (**b**) Absolute metabolite concentrations were compared between individuals for each subtype CD4+ or CD8+.

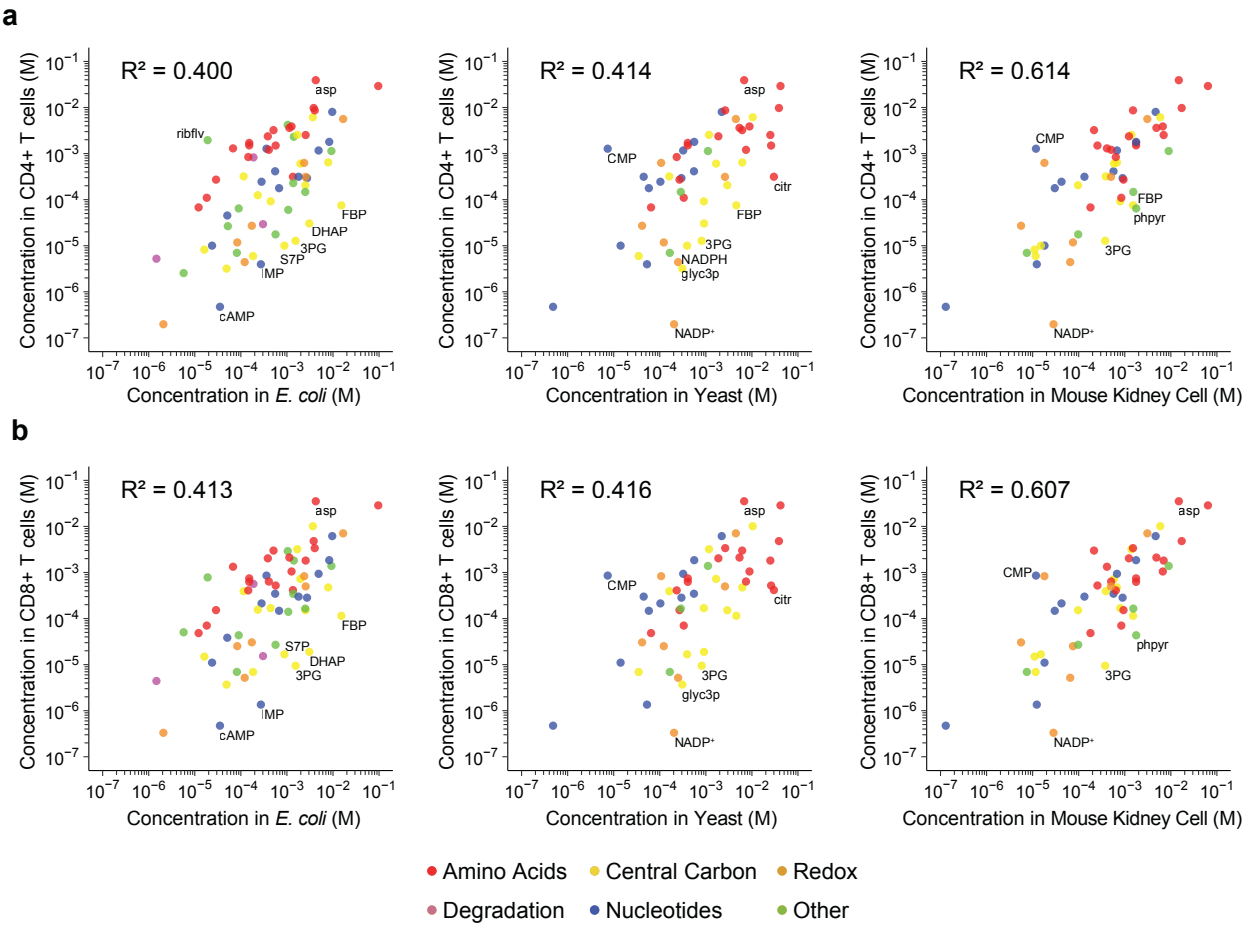

Extended Data Figure 4. Comparison of metabolomes between human primary T cells and other organisms. (**a**) Absolute metabolite concentrations in human primary CD4+ T cells were compared with those of *E. coli*, yeast, and iBMK cells. (**b**) Absolute metabolite concentrations in human primary CD8+ T cells were compared with those of *E. coli*, yeast, and iBMK cells.

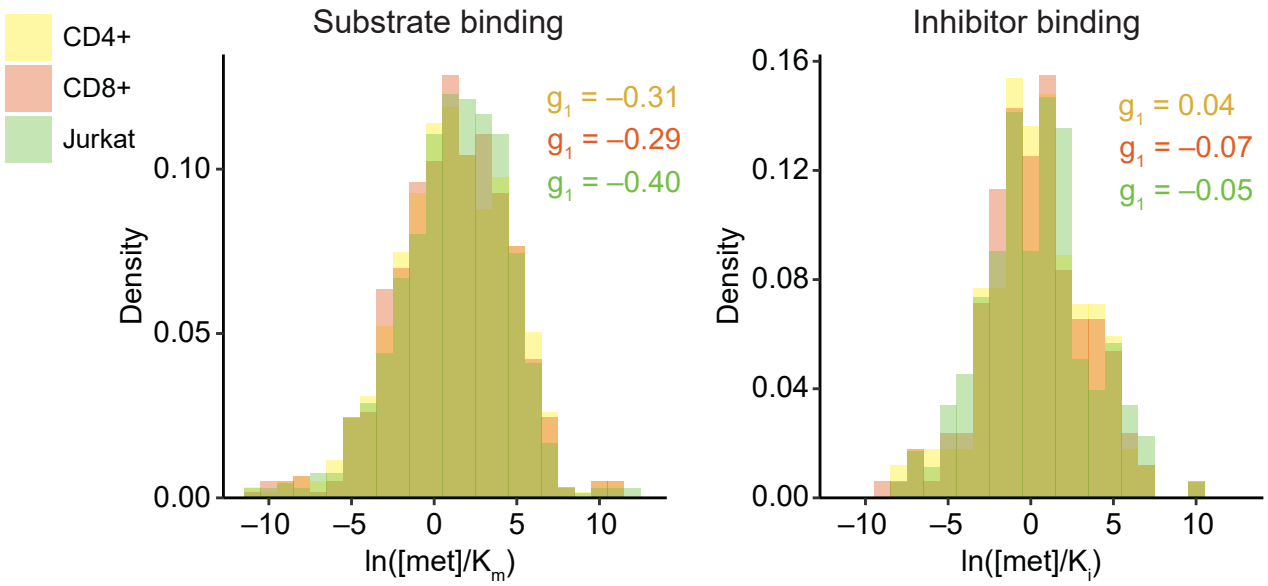

Extended Data Figure 5. Conservation of substrate and inhibitor binding site occupancy across T cell types. The Kolmogorov-Smirnov test on log ratios of metabolite concentrations to K_m and K_i concluded no significant differences between T cell types. g_1 represents the Fisher-Pearson moment coefficient of skewness for CD4+ (yellow), CD8+ (red), and Jurkat (green) T cells.

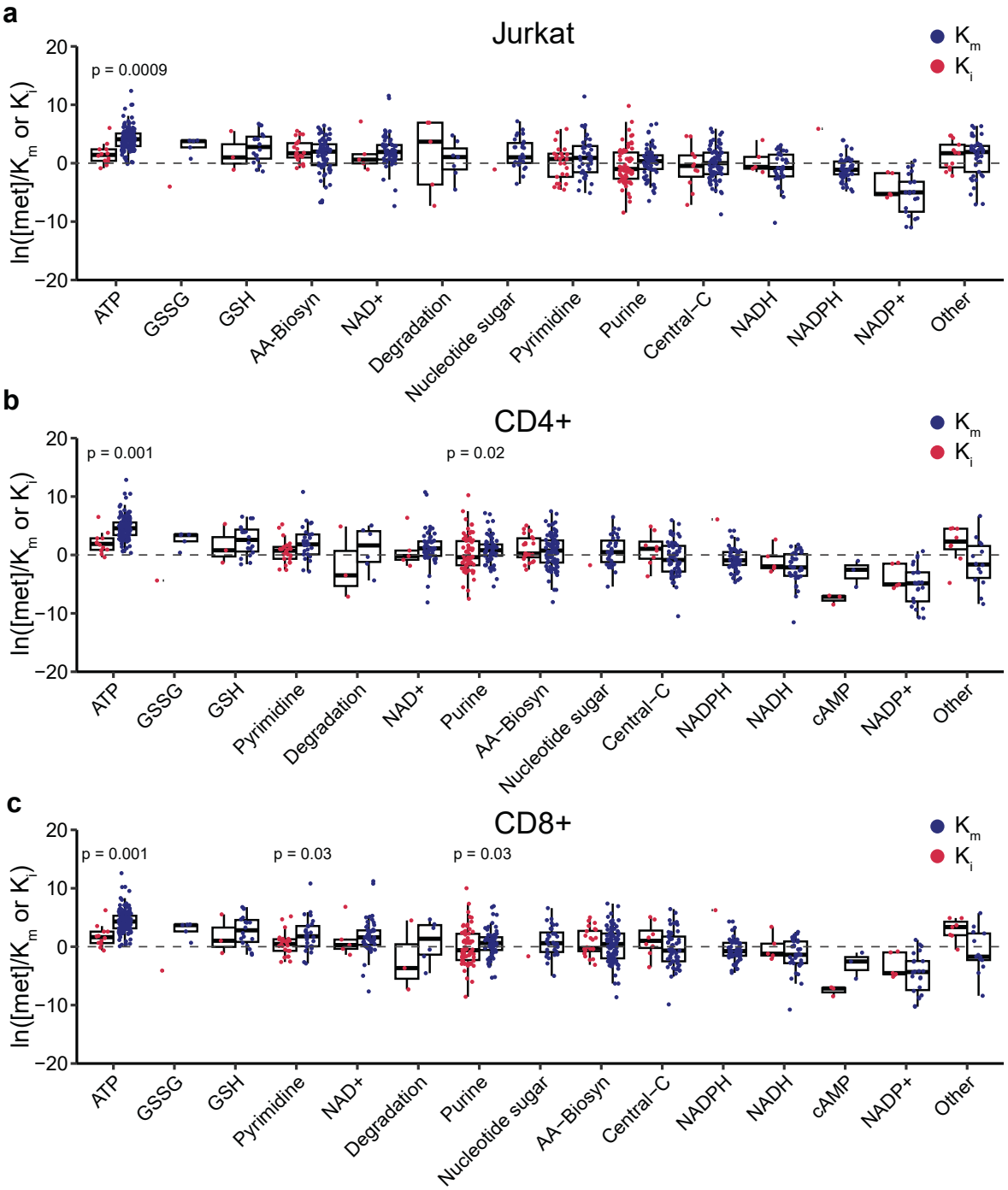

Extended Data Figure 6. Comparison of substrate and inhibitor binding site occupancy across metabolite groups. Substrate and inhibitor binding site occupancies were compared for individual metabolite groups in (**a**) Jurkat cells, (**b**) CD4+ human primary T cells and (**c**) CD8+ human primary T cells. Boxplots show boxes that extend from the first to third quartile, with thick lines representing the median. The whiskers extend to the farthest measurement values within 1.5 times the interquartile range from the edges of the box. Statistical significance for each metabolite group was assessed by the Kolmogorov-Smirnov test and multiple comparison correction using the Benjamini-Hochberg procedure.

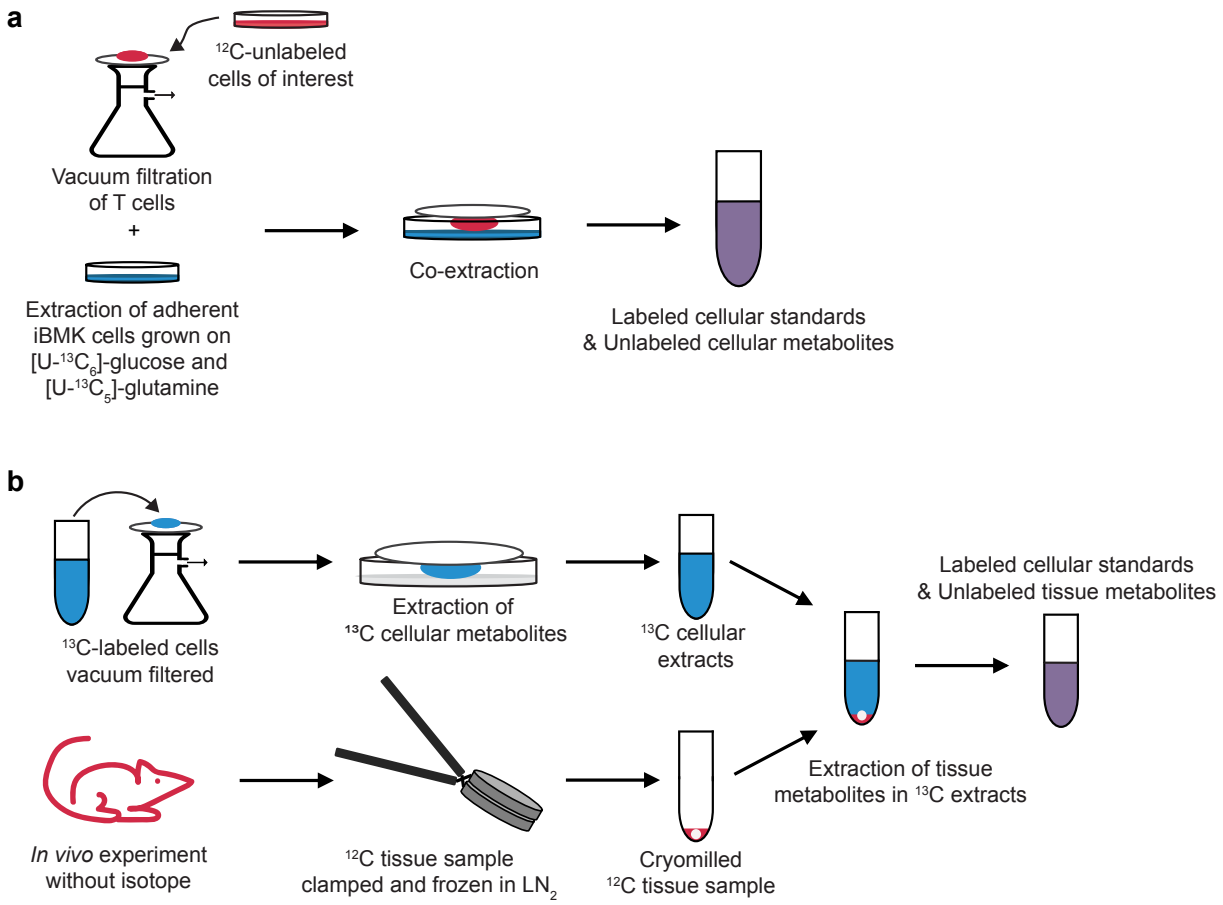

Extended Data Figure 7. Metabolite co-extraction methods for adherent cells and tissue samples. (**a**) iBMK cells were extracted on the plate they were grown on and T cells were extracted in the same plate after vacuum filtration. (**b**) Tissue samples clamped, snap frozen in liquid nitrogen (LN_2), and cryomilled can have their metabolites extracted using the extracts of ^{13}C-labeled reference cells.

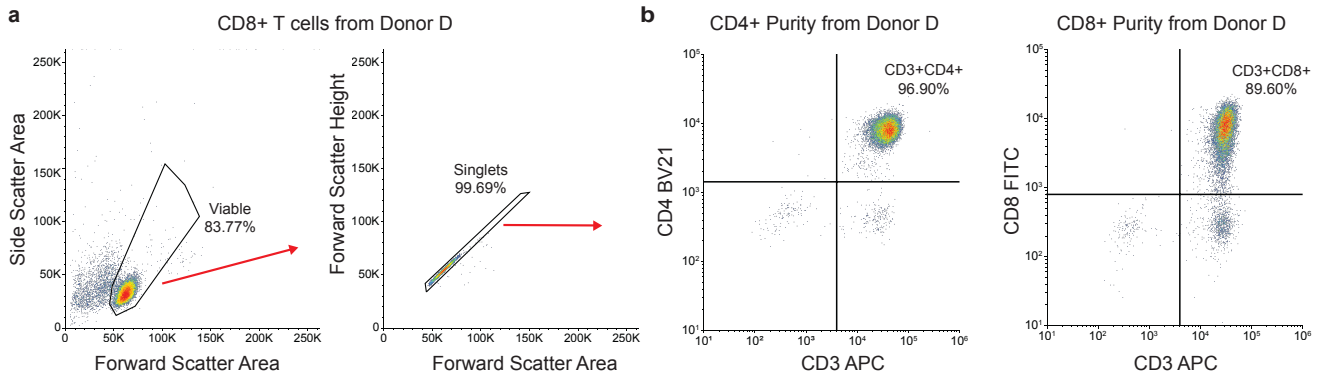

Extended Data Figure 8. Gating strategy for selecting viable cells and determining their subtypes. (**a**) Initial gating excluded debris by analyzing forward-scatter area (FSC-A) and side-scatter area (SSC-A) parameters. Doublets were then excluded using forward-scatter area (FSC-A) versus forward-scatter height (FSC-H). (**b**) The purity of the cell population was assessed by evaluating the singlets based on the fluorescence intensity of anti-CD4 and anti-CD8 antibody staining in conjunction with anti-CD3 antibody staining.

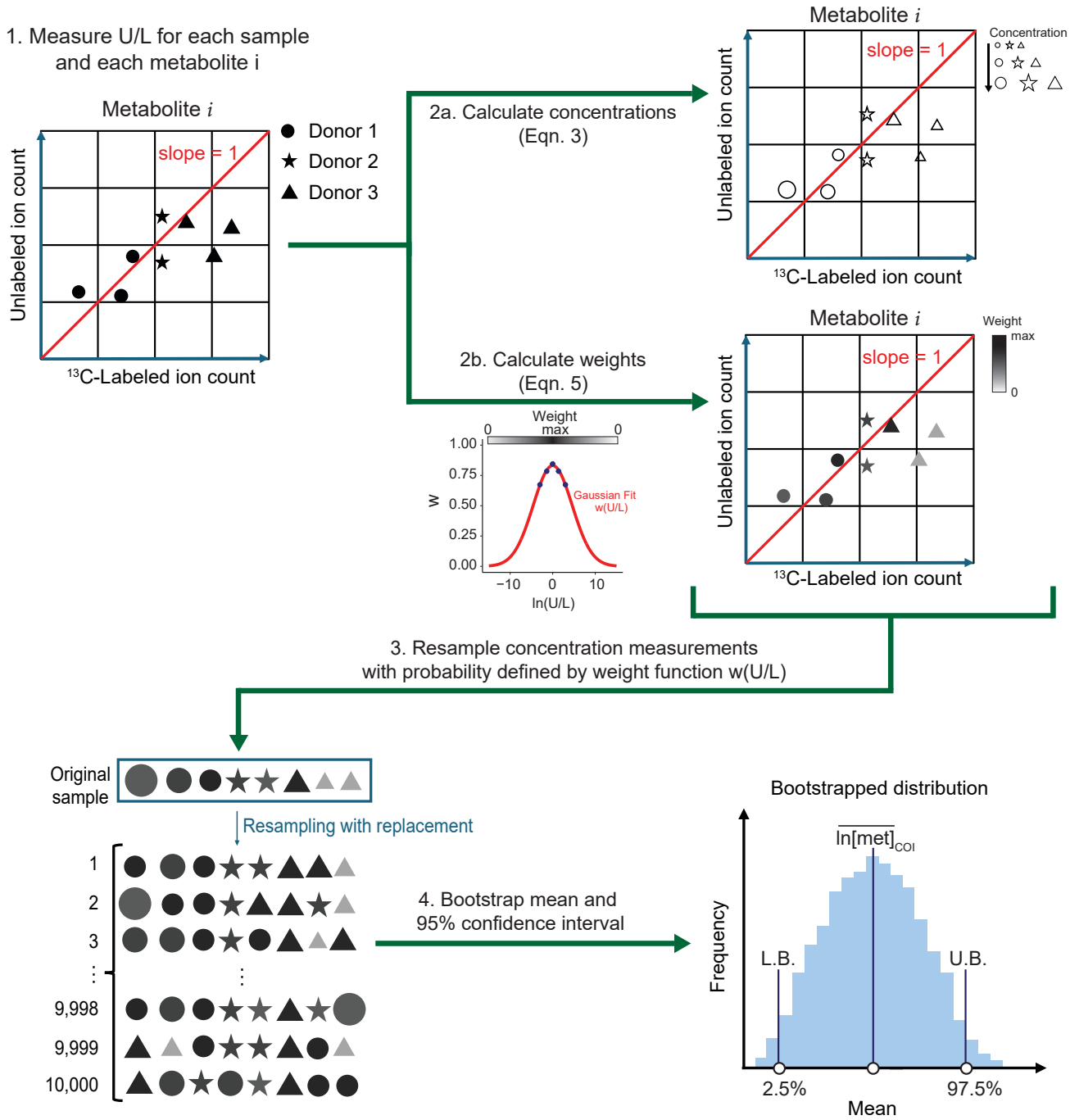

Extended Data Figure 9. Weighted bootstrapping for determining the distribution of log-concentrations of metabolites. A weighted bootstrapping approach was used to determine the mean and 95% confidence interval of each metabolite concentration. The Gaussian fit w(U/L) assigns a weight for resampling each metabolite concentration measurement using its associated U/L value. Log-concentration distributions were bootstrapped by resampling 10,000 means, each of which was calculated from weighted sampling of n (number of samples) log-concentration measurements with replacement. The bootstrapping method enabled the integration of multiple metabolite measurements.

658 **References**

659 1 O'Neill, L. A. & Pearce, E. J. Immunometabolism governs dendritic cell and macrophage
660 function. *Journal of Experimental Medicine* **213**, 15-23 (2016).
661 2 Nagarajan, S. R. *et al.* Lipid and glucose metabolism in hepatocyte cell lines and primary
662 mouse hepatocytes: a comprehensive resource for in vitro studies of hepatic metabolism.
663 *American Journal of Physiology-Endocrinology and Metabolism* **316**, E578-E589 (2019).
664 3 Pellerin, L. *et al.* Regulation of energy metabolism by neurotransmitters in astrocytes in
665 primary culture and in an immortalized cell line. *Glia* **21**, 74-83 (1997).
666 4 Bhakoo, K. K., Williams, S. R., Florian, C. L., Land, H. & Noble, M. D. Immortalization and
667 transformation are associated with specific alterations in choline metabolism. *Cancer*
668 *research* **56**, 4630-4635 (1996).
669 5 Ma, E. H. *et al.* Metabolic profiling using stable isotope tracing reveals distinct patterns of
670 glucose utilization by physiologically activated CD8+ T cells. *Immunity* **51**, 856-870. e855
671 (2019).
672 6 Britt, E. C., John, S. V., Locasale, J. W. & Fan, J. Metabolic regulation of epigenetic remodeling
673 in immune cells. *Current opinion in biotechnology* **63**, 111-117 (2020).
674 7 Hensley, C. T. *et al.* Metabolic heterogeneity in human lung tumors. *Cell* **164**, 681-694
675 (2016).
676 8 Axsom, J. *et al.* Quantification of nutrient fluxes during acute exercise in mice. *Cell*
677 *Metabolism* **36**, 2560-2579. e2565 (2024).
678 9 Bornstein, M. R. *et al.* Comprehensive quantification of metabolic flux during acute cold
679 stress in mice. *Cell Metabolism* **35**, 2077-2092. e2076 (2023).
680 10 Neinast, M. D. *et al.* Quantitative analysis of the whole-body metabolic fate of branched-
681 chain amino acids. *Cell metabolism* **29**, 417-429. e414 (2019).
682 11 Alseekh, S. *et al.* Mass spectrometry-based metabolomics: a guide for annotation,
683 quantification and best reporting practices. *Nature methods* **18**, 747-756 (2021).
684 12 Büscher, J. r. M., Czernik, D., Ewald, J. C., Sauer, U. & Zamboni, N. Cross-platform comparison
685 of methods for quantitative metabolomics of primary metabolism. *Analytical chemistry* **81**,
686 2135-2143 (2009).
687 13 Guder, J. C., Schramm, T., Sander, T. & Link, H. Time-optimized isotope ratio LC–MS/MS for
688 high-throughput quantification of primary metabolites. *Analytical Chemistry* **89**, 1624-1631
689 (2017).
690 14 Bennett, B. D., Yuan, J., Kimball, E. H. & Rabinowitz, J. D. Absolute quantitation of
691 intracellular metabolite concentrations by an isotope ratio-based approach. *Nature*
692 *protocols* **3**, 1299-1311 (2008).
693 15 Park, J. O. *et al.* Metabolite concentrations, fluxes and free energies imply efficient enzyme
694 usage. *Nature chemical biology* **12**, 482-489 (2016).
695 16 TeSlaa, T. *et al.* The source of glycolytic intermediates in mammalian tissues. *Cell*
696 *metabolism* **33**, 367-378. e365 (2021).
697 17 Lu, W. *et al.* Metabolite measurement: pitfalls to avoid and practices to follow. *Annual*
698 *review of biochemistry* **86**, 277-304 (2017).
699 18 Scherer, S. *et al.* Pyrimidine de novo synthesis inhibition selectively blocks effector but not
700 memory T cell development. *Nature immunology* **24**, 501-515 (2023).
701 19 Bennett, B. D. *et al.* Absolute metabolite concentrations and implied enzyme active site
702 occupancy in Escherichia coli. *Nature chemical biology* **5**, 593-599 (2009).

703 20 Lakhani, A. *et al.* Extracellular domains of CARs reprogramme T cell metabolism without
704 antigen stimulation. *Nature Metabolism*, 1-18 (2024).
705 21 Chapman, A. G., Fall, L. & Atkinson, D. E. Adenylate energy charge in Escherichia coli during
706 growth and starvation. *Journal of bacteriology* **108**, 1072-1086 (1971).
707 22 Romeu, M. *et al.* Evaluation of oxidative stress biomarkers in patients with chronic renal
708 failure: a case control study. *BMC research notes* **3**, 1-7 (2010).
709 23 Giustarini, D. *et al.* Pitfalls in the analysis of the physiological antioxidant glutathione (GSH)
710 and its disulfide (GSSG) in biological samples: An elephant in the room. *Journal of*
711 *Chromatography B* **1019**, 21-28 (2016).
712 24 Enns, G. M. *et al.* Degree of glutathione deficiency and redox imbalance depend on subtype
713 of mitochondrial disease and clinical status. *PloS one* **9**, e100001 (2014).
714 25 Valsecchi, F. *et al.* Metabolic consequences of NDUFS4 gene deletion in immortalized mouse
715 embryonic fibroblasts. *Biochimica et Biophysica Acta (BBA)-Bioenergetics* **1817**, 1925-1936
716 (2012).
717 26 Park, J. O. *et al.* Near-equilibrium glycolysis supports metabolic homeostasis and energy
718 yield. *Nature chemical biology* **15**, 1001-1008 (2019).
719 27 Noor, E. *et al.* Pathway thermodynamics highlights kinetic obstacles in central metabolism.
720 *PLoS computational biology* **10**, e1003483 (2014).
721 28 Macintyre, A. N. *et al.* The glucose transporter Glut1 is selectively essential for CD4 T cell
722 activation and effector function. *Cell metabolism* **20**, 61-72 (2014).
723 29 Zeng, H. *et al.* mTORC1 and mTORC2 kinase signaling and glucose metabolism drive
724 follicular helper T cell differentiation. *Immunity* **45**, 540-554 (2016).
725 30 Michalek, R. D. *et al.* Cutting edge: distinct glycolytic and lipid oxidative metabolic programs
726 are essential for effector and regulatory CD4+ T cell subsets. *The Journal of immunology*
727 **186**, 3299-3303 (2011).
728 31 Klein Geltink, R. I. *et al.* Metabolic conditioning of CD8(+) effector T cells for adoptive cell
729 therapy. *Nat Metab* **2**, 703-716 (2020).
730 32 Buck, M. D., O'sullivan, D. & Pearce, E. L. T cell metabolism drives immunity. *Journal of*
731 *Experimental Medicine* **212**, 1345-1360 (2015).
732 33 Buck, M. D. *et al.* Mitochondrial dynamics controls T cell fate through metabolic
733 programming. *Cell* **166**, 63-76 (2016).
734 34 Chang, C.-H. *et al.* Posttranscriptional control of T cell effector function by aerobic
735 glycolysis. *Cell* **153**, 1239-1251 (2013).
736 35 Sena, L. A. *et al.* Mitochondria are required for antigen-specific T cell activation through
737 reactive oxygen species signaling. *Immunity* **38**, 225-236 (2013).
738 36 Greiner, E. F., Guppy, M. & Brand, K. Glucose is essential for proliferation and the glycolytic
739 enzyme induction that provokes a transition to glycolytic energy production. *Journal of*
740 *Biological Chemistry* **269**, 31484-31490 (1994).
741 37 Pearce, E. L., Poffenberger, M. C., Chang, C.-H. & Jones, R. G. Fueling immunity: insights into
742 metabolism and lymphocyte function. *Science* **342**, 1242454 (2013).
743 38 Reina-Campos, M., Scharping, N. E. & Goldrath, A. W. CD8+ T cell metabolism in infection
744 and cancer. *Nature Reviews Immunology* **21**, 718-738 (2021).
745 39 Kishton, R. J., Sukumar, M. & Restifo, N. P. Metabolic regulation of T cell longevity and
746 function in tumor immunotherapy. *Cell metabolism* **26**, 94-109 (2017).

40 Siska, P. J. *et al.* Suppression of Glut1 and glucose metabolism by decreased Akt/mTORC1 signaling drives T cell impairment in B cell leukemia. *The Journal of Immunology* **197**, 2532-2540 (2016).
41 Crompton, J. G. *et al.* Akt inhibition enhances expansion of potent tumor-specific lymphocytes with memory cell characteristics. *Cancer research* **75**, 296-305 (2015).
42 Wu, B. *et al.* Mitochondrial aspartate regulates TNF biogenesis and autoimmune tissue inflammation. *Nature immunology* **22**, 1551-1562 (2021).
43 Franchi, L. *et al.* Inhibiting oxidative phosphorylation in vivo restrains Th17 effector responses and ameliorates murine colitis. *The Journal of Immunology* **198**, 2735-2746 (2017).
44 Zhao, Q. *et al.* CD4+ T cell activation and concomitant mTOR metabolic inhibition can ablate microbiota-specific memory cells and prevent colitis. *Science immunology* **5**, eabc6373 (2020).
45 Yin, Y. *et al.* (View at Publisher| View at, 2015).
46 Hackett, S. R. *et al.* Systems-level analysis of mechanisms regulating yeast metabolic flux. *Science* **354**, aaf2786 (2016).
47 Fell, D. & Cornish-Bowden, A. *Understanding the control of metabolism*. Vol. 2 (Portland press London, 1997).
48 Hope, H. C. *et al.* Coordination of asparagine uptake and asparagine synthetase expression modulates CD8+ T cell activation. *JCI insight* **6**, e137761 (2021).
49 Wu, J. *et al.* Asparagine enhances LCK signalling to potentiate CD8+ T-cell activation and anti-tumour responses. *Nature cell biology* **23**, 75-86 (2021).
50 Gnanaprakasam, J. R. *et al.* Asparagine restriction enhances CD8+ T cell metabolic fitness and antitumoral functionality through an NRF2-dependent stress response. *Nature Metabolism* **5**, 1423-1439 (2023).
51 Mills, E. L. *et al.* Succinate dehydrogenase supports metabolic repurposing of mitochondria to drive inflammatory macrophages. *Cell* **167**, 457-470. e413 (2016).
52 Mills, E. L. *et al.* Itaconate is an anti-inflammatory metabolite that activates Nrf2 via alkylation of KEAP1. *Nature* **556**, 113-117 (2018).
53 Seim, G. L. *et al.* Two-stage metabolic remodelling in macrophages in response to lipopolysaccharide and interferon-γ stimulation. *Nature metabolism* **1**, 731-742 (2019).
54 Young, J. D. INCA: a computational platform for isotopically non-stationary metabolic flux analysis. *Bioinformatics* **30**, 1333-1335 (2014).
55 O'Keeffe, S. *et al.* Bringing carbon to life via one-carbon metabolism. *Trends in Biotechnology* (2024).
56 Chen, W. W., Freinkman, E., Wang, T., Birsoy, K. & Sabatini, D. M. Absolute quantification of matrix metabolites reveals the dynamics of mitochondrial metabolism. *Cell* **166**, 1324-1337. e1311 (2016).
57 Piazza, I. *et al.* A map of protein-metabolite interactions reveals principles of chemical communication. *Cell* **172**, 358-372. e323 (2018).
58 Dixit, A. & Kalia, J. Protein-Metabolite Interactions: Discovery and Significance. *ChemBioChem* **24**, e202200755 (2023).
59 Kelley, L. P. *et al.* Integrated analysis of transcriptional and metabolic responses to mitochondrial stress. *Cell Reports Methods* **5** (2025).
60 Hatton, I. A. *et al.* The human cell count and size distribution. *Proceedings of the National Academy of Sciences* **120**, e2303077120 (2023).

61 Stanciu, L. A., Shute, J., Holgate, S. T. & Djukanović, R. Production of IL-8 and IL-4 by positively and negatively selected CD4+ and CD8+ human T cells following a four-step cell separation method including magnetic cell sorting (MACS). *Journal of immunological methods* **189**, 107-115 (1996).

62 Gutnick, D., Calvo, J. M., Klopotowski, T. & Ames, B. N. Compounds which serve as the sole source of carbon or nitrogen for Salmonella typhimurium LT-2. *Journal of bacteriology* **100**, 215-219 (1969).

63 Degenhardt, K. & White, E. A mouse model system to genetically dissect the molecular mechanisms regulating tumorigenesis. *Clinical cancer research* **12**, 5296-5304 (2006).

64 Rabinowitz, J. D. & Kimball, E. Acidic acetonitrile for cellular metabolome extraction from Escherichia coli. *Analytical chemistry* **79**, 6167-6173 (2007).

65 Wang, L. *et al.* Peak annotation and verification engine for untargeted LC–MS metabolomics. *Analytical chemistry* **91**, 1838-1846 (2018).

66 Seitzer, P., Bennett, B. & Melamud, E. MAVEN2: an updated open-source mass spectrometry exploration platform. *Metabolites* **12**, 684 (2022).

67 Schomburg, I. *et al.* BRENDA in 2013: integrated reactions, kinetic data, enzyme function data, improved disease classification: new options and contents in BRENDA. *Nucleic acids research* **41**, D764-D772 (2012).

68 Flamholz, A., Noor, E., Bar-Even, A. & Milo, R. eQuilibrator—the biochemical thermodynamics calculator. *Nucleic acids research* **40**, D770-D775 (2012).

69 Xu, H., Yang, D., Jiang, D. & Chen, H.-Y. Phosphate assay kit in one cell for electrochemical detection of intracellular phosphate ions at single cells. *Frontiers in Chemistry* **7**, 360 (2019).

70 Bevington, A. *et al.* A study of intracellular orthophosphate concentration in human muscle and erythrocytes by 31P nuclear magnetic resonance spectroscopy and selective chemical assay. *Clinical Science* **71**, 729-735 (1986).

71 Behjousiar, A., Kontoravdi, C. & Polizzi, K. M. In situ monitoring of intracellular glucose and glutamine in CHO cell culture. *PLoS One* **7**, e34512 (2012).

72 Bearham, J., Garnett, J. P., Schroeder, V., Biggart, M. G. & Baines, D. L. Effective glucose metabolism maintains low intracellular glucose in airway epithelial cells after exposure to hyperglycemia. *American Journal of Physiology-Cell Physiology* **317**, C983-C992 (2019).

73 Xu, J., Huang, P., Qin, Y., Jiang, D. & Chen, H.-y. Analysis of intracellular glucose at single cells using electrochemiluminescence imaging. *Analytical chemistry* **88**, 4609-4612 (2016).